

ACTA TECHNICAJAURINENSIS

Vol. 17, No. 2, pp. 59-64, 2024 10.14513/actatechjaur.00716



Research Article

The Impact of Odd-Even Policy on Travel Distance and Time in Private Sector

Agung Chandra^{1*}

¹Department of Industrial Engineering, Universitas Mercu Buana Jalan Raya Meruya Selatan no.1, Jakarta 11650, Indonesia *e-mail: agung.chandra@mercubuana.ac.id

Abstract:

Government of Jakarta has struggled to mitigate the traffic congestion by implementing the odd-even policy. This policy has restricted some roads for vehicles to pass in Jakarta in a certain time and this policy needs to be studied further for its impact on distance and time, especially for private companies. The research was conducted in private sectors which its warehouse located in Tangerang and its customers spread in Jakarta, Bogor, Depok, Tangerang and Bekasi. The study focuses on 49 routes that every route had some customers' location. The sequence for every route was determined if had a shortest distance and/or fastest time with the help of optimoroute software. Then, every route was processed by Google Maps both in normal condition and odd-even policy's condition in order to get the distance and travel time. The results indicated that around 44.89% of routes have further distance and 16.55% have longer time, these results mean costlier for private companies since odd-even policy has been implemented. The study also compared two alternatives between maintaining current condition and switching to rent a vehicle with third party logistics, the result indicated that maintaining current condition alternative was still beneficial than switching to rent a vehicle alternative.

Keywords: Odd-even policy; impact; optimoroute; google maps

I. Introduction

Congestion in developing countries such as Indonesia is associated with limited road infrastructure and lack of traffic management resources. There are many causes of traffic congestion such as subsequent increase in private vehicle ownership [1], the state of the roads and driving habits, insufficient information available on traffic condition, and institutional problems [2], wrong parking, disobedience to traffic rules (human factors) [3].

Table 1 showed us that number of motor vehicle has been increasing around five percent every year for all types: passenger car, bus, truck, and motorcycle [4], apart from year 2020. During the year 2020, the increment of motor vehicle was around two percent, this was because of pandemic

era. This increment made road more congested, because the average increment of road length was relatively near zero percent in Jakarta and Banten. Congestion can cause unpredictable journey times, stress, or anger (psychological discomfort), wasting fuel, tiredness, being late for appointment [5]. Congestion could be eased by prohibiting a portion of the existing fleet of vehicle from circulating without infringing on the right to buy vehicles.

There were some steps that Indonesian government has already implemented, such as three-in-one policy which was revoked in 2016 because of car jockey practices [6], U-turn reduction, increasing number of public transportation such as busway, and odd-even policy which allows odd number plate pass the roads on odd date and even number plate pass the road on even date, specifically 4-wheeled vehicles [7].

Province	Motorvehicle	2018	2019	2020	2021	2022
Jakarta	Passenger car	3,082,616	3,310,426	3,365,467	3,544,491	3,766,059
	Bus	33,419	34,905	35,226	36,339	37,180
	Truck	631,156	669,724	679,708	713,059	748,395
	Motorcycle	15,037,359	15,868,191	16,141,380	16,711,638	17,304,447
	Total	18,786,568	19,885,265	20,223,801	21,007,548	21,858,103
Banten	Passenger car	209,212	227,547	232,939	247,020	264,447
	Bus	3,254	3,466	3,519	3,573	3,615
	Truck	70,098	75,374	76,905	82,260	87,934
	Motorcycle	1,991,810	2,161,809	2,234,539	2,371,748	2,514,383
	Total	2,274,374	2,468,196	2,547,902	2,704,601	2,870,379
Indonesia	Passenger car	14,838,106	15,600,108	15,803,933	16,413,522	17,175,632
(country)	Bus	223,011	231,717	233,406	237,829	241,215
	Truck	4,804,178	5,029,305	5,090,625	5,299,603	5,528,669
	Motorcycle	106,836,985	112,950,332	115,188,762	120,045,878	125,267,349
	Total	126,702,280	133,811,462	136,316,726	141,996,832	148,212,865

Government of Jakarta, capital city of Indonesia has implemented the odd-even policy in 2019 to mitigate congestion, air pollution that caused by road traffic [9], and density of road [10]. From the perspective of private sector, this policy restricted the shipment activities, because the vehicle could not be operated from Monday to Friday on a certain time, 06 to 10 WIB and 16 to 21 WIB, except for vehicle with sticker of disability, ambulance, fire fighter vehicle, public transportation with yellow plate, motorcycle, electric vehicle, fuel truck, vehicles of high ranking state officials, etc., therefore there was an interruption for shipping the customer's order and an organization had to deal with it. There were some solutions to deal with this time restriction. The first one was dealing with current condition by using existing vehicle. If the vehicle plate number was different with date, then the route must be changed in order to avoid the restricted roads which the distance of route and time needed may be longer. Longer time may cause driver work overtime. In this case, we had to calculate the variance between cost that incurred during and outside odd-even operating hours, and the lowest cost will be chosen. The second one, the organization would replace all private vehicles with public vehicles that have yellow plate number, in other words, the organization had to rent vehicles to third party logistics. In this option, there would be a rental cost per month that organization had to pay. The third one was to buy additional vehicles with even or odd number of plate. Consequently, there would be idler vehicles and the organization did not plan to expand its business now because the average capacity of vehicle used was around 70%. Therefore,

the third option was not being considered. Things to note, the organization did not consider buying the new vehicle, because private organizations could not determine the odd or even number of vehicle plate. The first and the second solution would be studied further in this research.

The aim of this research was to study the impact of odd-even policy implementation on distance, time and cost that incurred in private sector. The study of travel distance and time would be taken from warehouse as a starting point that was located in Tangerang to its customers that located in Jakarta, Bogor, Depok, Tangerang, Bekasi (Jabodetabek) by using OptimoRoute software and Google Maps.

II. MATERIALS AND METHODS

1. DISTANCE AND TIME VARIANCE

Google Maps as an online map service was used to calculate the distance of route for both car and public transport [11]. There were two conditions that we had to know:

- a. The distance and time needed during odd even operating hours which vehicle can only go through on the restricted roads.
- The distance and time needed that out of odd even operating hours which vehicle can go through on all roads or called unrestricted roads.

The distance variance between these two conditions were converted to cost. The formulae are similar to seen at Ruth et al [12].

 $Fuel\ cost = Fuel\ price\ x\ distance\ variance\ x$ $consumption\ rate \qquad \qquad (1)$

where:

Consumption rate = Litre per kilometre

Distance variance = Kilometre

Price of fuel = EUR 0.41 per litre (subsidized solar), this was the price as of September 1st, 2023.

The distance of route followed the concept of travelling salesman problem (TSP) which the goal is to find the shortest distance by visiting all cities (locations of customers) and returning to the starting point [13], and the starting point will be the same with the ending point, in other words, the vehicle started from warehouse, shipping goods to customer's destinations and returned to warehouse again. The distance was not symmetric (asymmetric) because the route followed the real distance from Google maps.

The time variance between these two conditions were also converted to cost that we called labor cost.

Labor cost = Labor rate x time variance (2)

where:

Labor rate = EUR per hour, which minimum wage in Tangerang, Banten was EUR 274.6 per month. Time variance = hour(s)

$$Total\ cost = Fuel\ cost + Labor\ cost \tag{3}$$

Other factors that may influence time variance are parking, pedestrian crossing, turn like U-turn, all of these are common conditions [14] in Jakarta.

2. ECONOMIC ANALYSIS: RENT VS DO NOTHING

In this research, the organization had two alternatives, one was rent a yellow plate vehicle from third party logistics (3PL) company and another one was do nothing. Do nothing alternative means, the organization has to avoid odd-even roads and may get a longer distance or/and longer time when shipping goods to customers. The factors that may contribute to a longer distance and time could be a slower speed in a narrower road, further road, traffic congestion, and unfamiliar knowledge of driver. These two alternatives would be compared, and the organization would choose the lowest cost. **Fig. 1** shows the framework of research.

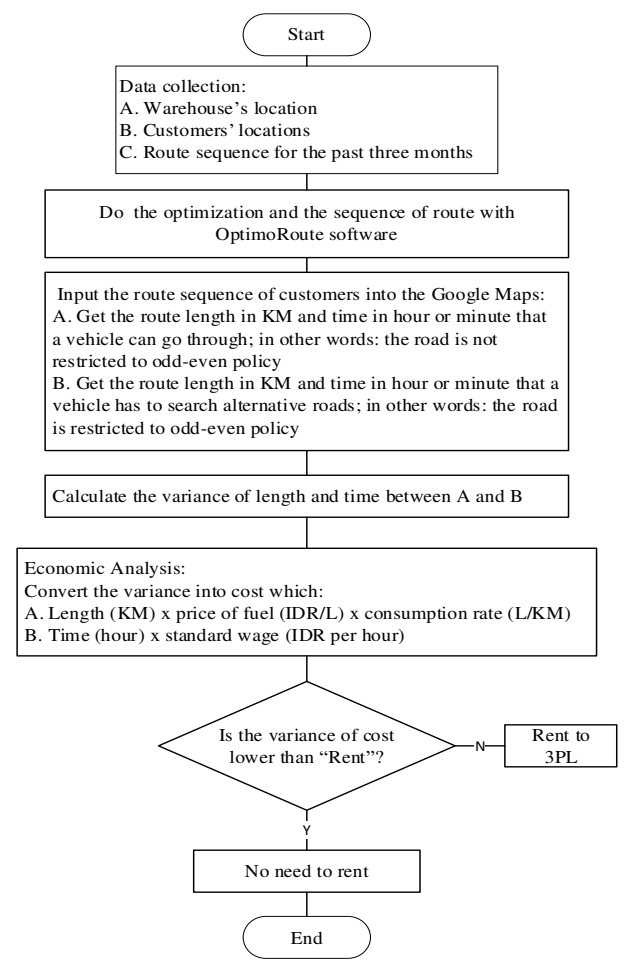


Figure 1. Framework of Research

3. DATA AND ASSUMPTION FOR THIS RESEARCH

There were some data needed for optimoroute software, and this data must be prepared:

- a. Customer and warehouse's location, a detail address. The objective was to get accurate location, so this accurate location would produce accurate distance.
- b. Location name, in this section, one can choose customer's shop or customer name.
- c. Number of drivers who would deliver the products to customer's location, this helped route planner get a group of locations of customers that had to be delivered for one vehicle.

Some data were needed for further analysis:

- a. Monthly wage of driver
- b. Current price of fuel
- c. Toll road cost that passed when delivery
- d. Current rental cost

There were some calculations in this research that based on these assumptions:

- a. Average working hours per day is 8 hours and there are 5 working days per week.
- b. The amount of working hours per month = 52 weeks per year x 40 working hours per week: 12 months = 173 hours.

c. The wage rate per hour = EUR 1.59

These assumptions based on Labor Laws, Undang—Undang Ketenagakerjaan nomor 13 tahun 2003. The starting point was from warehouse and the route was ended in warehouse. Before using the Google Maps, the sequence of customer's locations in one route was determined by the software OptimoRoute.

4. OptimoRoute SOFTWARE

OptimoRoute is regarded as one of the suitable software for solving vehicle routing problem and mobile workforce that has following advantages: high ease of use, the clarity with which solutions are shown, both graphically and analytically, through the use of colours and the sense of the streets, and the high amount of data from the different routes illustrated in the solutions (**Fig. 2**). OptimoRoute is a routing optimization software, created in 2012 in the United States, used by multiple companies from different business sectors around the world [15, 16].

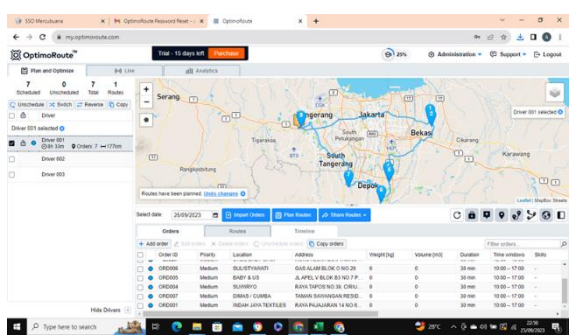


Figure 2. Planning & Optimizing Routes by optimoroute software

III. DATA ANALYSIS AND RESULTS

The shipment data for this research was collected for three months from July to September 2023, working days, Monday to Friday started from 08:30 to 17:30. The average routes were 49 per months and available during observation, all routes started from warehouse, Jatiuwung, Tangerang and at the end, returned to warehouse, Tangerang. Here are the customer's data: 8 in Tangerang, 61 in Jakarta, included expedition, 5 in Depok, 4 in Bekasi, and 1 in Bogor. This following Table 2 showed us that there were two effects emerged when odd-even policy was implemented, further distance and longer travel time. Further distance means the odd-even policy has made a driver search and pass through unrestricted roads, further distance also means more fuel was consumed. Longer time means the odd-even policy has made a driver pass through unrestricted roads, but the velocity could not exceed 40 KM per hour. Longer time means there was an additional time for driver to work.

Table 2. The impact of odd-even policy on distance and time

Routes	Value

Further distance	22	137.5 KM
Longer time	8	5h 7m 0s

Fig. 3 was the example when odd-even policy implemented then further distance happened, even only a little bit.

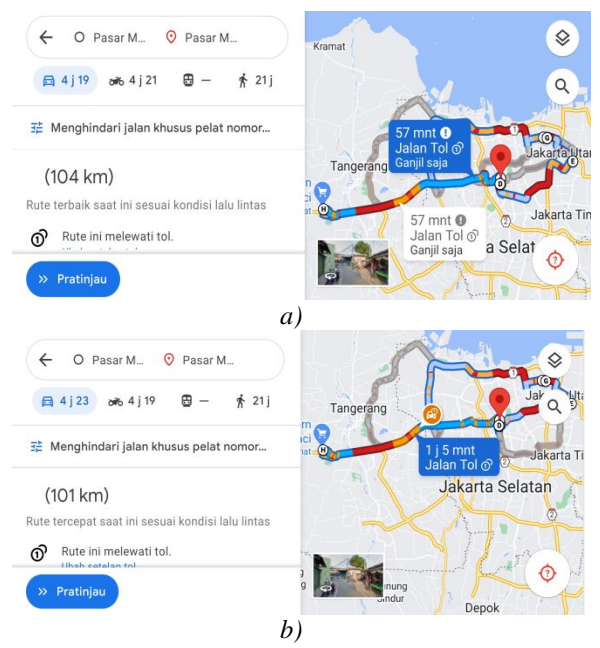


Figure 3. The odd-even a) policy implemented b) policy not implemented

1. Routes - Further distance

The impact of odd-even policy could make the route further because some roads were restricted by odd-even policy, then driver had to look for and took another road. From 49 routes per month, there were 22 routes (44.89%) had further distance, the total was 137.5 Kilometre. Average Kilometre per Litre was 5.8, and fuel price was EUR 0.41 per little. The fuel was solar that subsidized by government, then the cost incurred per month that caused by odd-even policy:

$$\frac{137.5 \ KM}{5.8 \ KM/L} xEUR \frac{0.41}{L} = EUR \ 9.71/month$$

2. Routes – Longer time

The impact of odd-even policy also made the travel time longer. Longer time was caused by narrower road so that a driver could not drive a vehicle more than 40 KM per hour and driver had to look for the unrestricted roads at the time. Other factor was further distance. From 49 routes, there were 8 routes (16.33%) had longer time, the total were 5 hours 7 minutes, then it would cost:

5.12 hours x EUR 1.59 per hour = EUR 8.14 per month

Then, total cost incurred per month by the odd-even policy = EUR (9.71 + 8.14) = EUR 17.85 per month

3. Comparison between Rent vs Current Condition

It was important to compare the total cost between current condition and rent a vehicle.

Table 3. Cost comparison

	Average cost (EUR) per
	month
Current condition:	
- Cost incurred by odd-	17.85
even policy	
- Fuel cost 600 Litre	244.30
- Wage of driver	274.60
- Holiday allow. +	35.90
overtime	
- Toll road cost	5.98
- Maintenance cost	29.90
- Administrative cost	11.98
- Insurance cost	20.97
Total cost	631.77
Rent a vehicle with 3PL	1,197.60

Table 3 indicated that cost for current condition was still cheaper than rent a vehicle, so that the private companies does not need to switch to vehicle rental and drop the current vehicles. The organization could save about EUR 565.83 per month.

In this study, it is obvious that, the odd-even policy implementation in Jakarta city had not a big impact on distance and time when delivered finished goods from Tangerang to its customers in Jabodetabek, the reasons were:

- There were customers' locations that could be delivered by taking the toll road and were not restricted by odd-even policy: North Jakarta such as Sunter, Kelapa Gading, Ancol; Tapos, Depok; Tangerang areas; Bogor.
- Delivered at outside of odd-even hour limits, from 10 to 16.

4. Discussion and Future Research

REFERENCES

- [1] N. Bashingi, M. Mostafa, D.K.Das, The State of Congestion in The Developing World; The Case of Gaborone, Botswana, Transportation Research Procedia 45 (2020) pp.434-442.https://doi.org/10.1016/jtrpo.2020.03.036
- [2] A. Bull, et.al, Traffic Congestion: The problem and How to Deal with It, United Nations, 2003.
- [3] S. Iro, E.C.P. Mbano, Causes of traffic congestion; a study of Owerri municipal area of IMO state, American Journal of Environmental

In this study, there was still some aspects that a researcher can do in the future. Government of Jakarta has planned to implement Electronic Road Pricing (ERP). ERP was viewed as a tool to restrict motor vehicle by electronic system at certain roads and certain time. From this, one can further compare some options: do nothing versus ERP. One can also do the research about the factor that influence most on driving time, whether length of road, route, parking, pedestrian crossing, or may be turn like Uturn.

IV. CONCLUSIONS

The odd-even policy had an impact on travel distance and time. There were around 44.89% of routes that had further distance and around 16.33% had longer time. The total cost at current condition, do nothing on odd-even policy saved EUR 565.83 than rent a vehicle at 3PL, it was still beneficial for the company to maintain current condition than to switch to rent a vehicle from third party logistics (3PL). In the future, one can do research about benefit and limitations of Electronic Road Pricing (ERP).

ACKNOWLEDGEMENT

The publishing of this paper was supported by Universitas Mercu Buana, Jakarta, Indonesia.

AUTHOR'S CONTRIBUTIONS

A. Chandra: Conceptualization, Literature review, Data collection and Experiments, Analysis, Writing and Review.

DISCLOSURE STATEMENT

The authors declare that they have no known competing financial interests or personal relationships that could have appeared to influence the work reported in this paper.

ORCID

Agung Chandra https://orcid.org/0000-0002-0338-1588

- Sciences 18 (3) (2022) pp.52-60. https://doi.org/10.3844/ajessp.2022.52.60
- [4] Badan Pusat Statistik, Statistical yearbook of Indonesia 2023, Chapter 10, BPS-Statistics Indonesia, 2023.
- [5] Organization for Economic Co-Operation and Development, Managing Urban Traffic Congestion, OECD publishing (2007) pp.1-296.

- [6] E. Prasojo, A.A. Salam, DKI Jakarta's Odd-Even Transportation Policy Formulation from The Perspective of Evidence Based Policy, Policy & Governance Review Vol.6 (1) (2021), pp.40-57. https://doi.org/10.30589/pgr.v6i1.439.
- [7] N. Tinumbia, K. Khotimah, The Impacts of Odd-Even Restriction Policy on Travel Behaviour, Jurnal Infrastruktur 7 (1) (2021) pp.21-28.
- [8] Statistical yearbook of Indonesia 2021-2023
- [9] B. Csonka, Data Driven Analysis of Transport and Weather Impact on Urban Air Quality, Acta Technica Jaurinensis 10 (3) (2023) pp.99-106. https://doi.org/10.14513/actatechjaur.00698.
- [10] Pemprov DKI Jakarta, KebijakanGanjilGenap (2023) [cited 2023-08-22]. https://www.jakarta.go.id
- [11] K. Viergutz, D. Krajzewicz, Analysis of the Travel Time of Various Transportation Systems in Urban Context, International Scientific Conference on Mobility and Transport Urban Mobility – Shaping the Future Together, TUM2018, Munich, Germany, 2018, pp.1-9

- [12] M. Ruth, T.A. Timbario, T.J. Timbario, M. Laffen, Methodology for Calculating Cost per Mile for Current and Future Vehicle Powertrain Technologies with Projections to 2024, NREL, Detroit, 2011.
- [13] A. Chandra, C. Natalia, Application of Multiple Traveling Salesman Problem on Zone Picking, Academic Journal of Manufacturing Engineering Vol. 21, Issue 1 (2023) pp.51-58.
- [14] S. Bajcetic, P. Zivanovic, S. Tica, B. Milovanovic, Factors Influencing Driving Time in Public Transport: A Multiple Regression Analysis, Traffic and Transportation 35(1), pp.37-54. https://doi.org/10.7307/ptt.v35i1.29
- [14] A. Chandra, C. Natalia, The Effect of Queue on Delivery Time , Nauchno-tekhnicheskiy vestnik Bryanskogo gosudarstvennogo universiteta no.3 (2023). https://doi.org/10.22281/2413-9920-2023-09-04-279-286
- [15] OptimoRoute, Inc, 2023, USA. https://optimoroute.com/



This article is an open access article distributed under the terms and conditions of the Creative Commons Attribution NonCommercial (CC BY-NC 4.0) license.

ACTA TECHNICA JAURINENSIS



Vol. 17, No. 2, pp. 65-74, 2024 10.14513/actatechjaur.00729



Research Article

Analysis of Normative Requirements and Technical Specifications of a Structural Design of the Mechanical Device Operating in the Amusement Industry

Denis Molnár^{1,*}, Miroslav Blatnický¹, Ján Dižo¹, Sebastián Solčanský¹, Dávid Čierňava¹

¹Department of Transport and Handling Machines, Faculty of Mechanical Engineering, University of Žilina Univerzitná 8215/1, 010 26 Žilina, Slovak Republic *e-mail: denis.molnar@fstroj.uniza.sk

Submitted: 21/12/2023 Accepted: 01/03/2024 Published online: 14/03/2024

Abstract:

In current hectic times, people should be able to slow down and diversify their free time. Therefore, the contribution of the amusement industry should not be negligible but, on the contrary, should be seen as something where whole families can seek respite from ordinary worries and problems. For this reason, the presented paper was written, which represents an intermediate step in the design of an amusement facility suitable for amusement parks that respects the normative requirements. Technical standardization represents a set of rules, characterizations, guidelines, and results of activities necessary for mutual understanding when solving technical problems in production. Adherence to standards is essential when launching a product on the market. The main standard indicating the full functioning of an amusement device is STN EN 13814. Its analysis and the resulting technical specifications of the proposed equipment are the chief objectives of the paper.

Keywords: Amusement ride; Design; CAD (Computer-Aided Design) model; Standards; Specifications

I. Introduction

The object of standard STN EN 13814-1 and ISO 17842-1 standard is to specify the minimum requirements necessary to ensure the safe design, calculation, manufacture, assembly, maintenance, operation, inspections, and testing of mobile, temporary or permanently installed machinery and structures such as roundabouts, swings, flat rides, Ferris wheels, roller coasters and other amusement handling machines [1,2]. The mentioned devices must be intended for repeated installation without damage to the features or loss of integrity in temporarily or permanently operated amusement parks, funfairs, and any other places suitable for use.

The basic design rule is the safety of the occupants. Thus, the permissible gravity accelerations resulting from the standard must be considered at first [3,4]. The standard STN EN 13814 prescribes that the acceleration due to gravity acting on passengers must not exceed 6g. The reference point for the calculated and measured accelerations is 60 cm above the seat level. The maximum deceleration must not exceed 0.7g for emergency brakes and 0.5g for normal stopping brakes. The dimensions of seats

and gondolas are designed with regard to the forces from self-weight, adverse loads and motion.

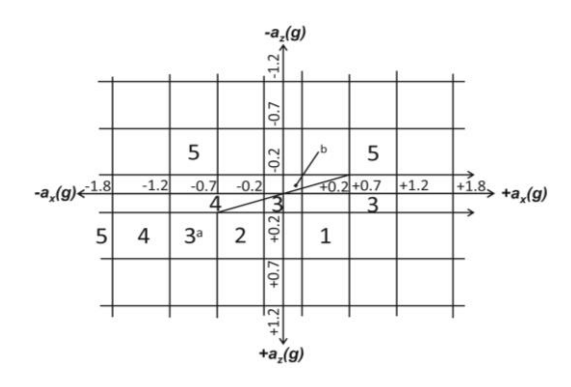


Figure 1. Areas of application of restraint devices [3]

As stated in STN EN 13814, all seats of amusement rides must be equipped with the necessary spine supports at least 0.4 m high. Moreover, the seat surface must have an appropriate slope towards the spine support. For the sake of the safety of passengers, seats fixed next to each other on the gondola should be designed in order that the minimum seat outline distance is 0.5 m. A safety factor of $\gamma = 6$ (-) is required in the dimensioning and designing of the seats [2,4]. On the basis of the acceleration acting on the occupants, we can design

suitable restraint devices to ensure sufficient restraint and safety in the course of the ride (**Fig. 1**). Minimum requirements:

- Area 1 no restraint devices are required;
- Area 2 restraint for two or more passengers, manual device, optional backup, with nonadjustable restraint position;
- Area 3 restraint for two or more occupants, manual restraint manipulated by operator or attendant, individually with adjustable restraint position;
- Area 4 individual device for each passenger, automatically restrained in the operating position, individually with adjustable restraint position;
- Area 5 individual device for each passenger, automatic restraining in operating position with check of restraint, unlocking by means of central system, with warning signal (light or sound), functional restraining required [2,16].

Motorized restraint devices can create additional hazards. Therefore, their movement must be sufficiently decelerated, and the maximum force measured at the edge of contact of the device must not exceed 150 N. Before restraint is initiated, electrically controlled restraint devices are equipped with a safety light system or an audible safety system to warn that the restraint is fully operational; thus, riding can commence [13-15;17].

II. PROPOSED AMUSEMENT RIDE

The authors decided to develop the amusement device with a changeable tilt of raising (arm raises horizontal platform) during rotation (**Fig. 2**).



Figure 2. Proposed amusement device with changeable tilt in the course of lifting

Passengers are seated in gondolas that are fixed to a steel structure. The wheel is spun through an electric motor, which is mounted on top of the main beam. The motor spins the structure by means of a gear train, where a pinion is the driving member and a large gear wheel attached to the structure mounting is the driven member. The entire structure is erected by means of hydraulic system and a 90° change in

the position of the device is achieved. The process of lifting occurs only at a condition where the wheel reaches a maximum rotational speed of 14 rpm. The passengers experience a maximum gravitational acceleration of approximately 2.2g. The achieved wheel rotational speed ensures that the gondolas can be deflected by up to 53° after reaching the maximum speed before lifting begins.

Passengers must be secured with a restraining device in the course of riding, inasmuch as during lifting can occur a state when passengers going upside down. Due to the fact that the attraction is fully demountable, the operator is able to transport it between amusement parks or between smaller festivals where the amusement equipment is present. The mentioned amusement ride can be classified as a classic family amusement ride [9-12].

The primary assumption when designing the model of this handling device was that the wheel should rotate clockwise with a speed of $n_k = 14$ rpm. Analytical calculations are performed with regard to the maximum weight from passengers $m_{Pmax} = 3600$ kg. In terms of determining other specifications, it was necessary to choose for what number of passengers the attraction will be designed, and the required components that are essential for the proper operation and safe functioning of the attraction [5-7]. The other selected units will be designed using analytical calculations or software [18,19]. The chief specifications describing the equipment are divided into three groups:

- 1. Specifications intended for passengers;
- 2. Specifications intended for the operator;
- 3. Special specifications.

Passenger specifications should be displayed at each amusement ride on an information board for the reason that passengers can familiarise themselves with the type of operation or ride parameters before riding [6,14]. The selected parameters are:

- the number of passengers that the attraction carries in one ride $-n_p = 36$ (-);
- rotational speed of the wheel $-n_k = 14$ rpm;
- period of acceleration t_r = 17 s;
- time of lifting to vertical position $-t_z = 30 \text{ s}$;
- time of a ride $-t_j = 2$ min;
- age or height restrictions (persons must be older than 8 years and taller than 135 cm, restrictions must be met simultaneously);
- electric passenger restraint with additional manual restraint.

In addition to the above specifications, we specify additional specifications that must be known by the operator for proper care of the attraction, installation or dismantling:

- 1. number of gondolas $n_g = 18$ (-);
- 2. number of trusses (truss construction) $n_l = 18$ (-);
- 3. motor power $P_m = 90 \text{ kW}$;

- 4. number of cylinders in the telescopic hydraulic system $n_v = 3$ (-);
- 5. the pressure applied to the telescopic system -p = 35 MPa;
- 6. extension of the telescopic system h_{cp} = 4.8 m;
- 7. total length of the telescopic system $h_{ct} = 6.96$ m:
- 8. the area required for the installation of the device $-S = 250 \text{ m}^2$.

The maximum number of starts is proposed only as an indicative value, which should not exceed 200 starts per day. Thus, the total time of operation per day (7 hours) with breaks during boarding or disembarking passengers is provided by means of time of the ride multiplied by the maximum number of starts. The operator must only start the amusement machine when the attraction is as full as possible, the minimal occupation is when at least 1/4 of the circumference of the wheel is occupied. The distribution of passengers must be as even as possible around the circumference in order that the wheel is well balanced. Special specifications set out the main physical characteristics of the attraction [7,12,14]. We use formulae (1) to (7) to find these physical characteristics that affect the structure or the passengers. The period T is represented as a material point, in other words, 1 gondola occupied by passengers, which describes the circle 1 time. The formula (1) is used for the period *T*:

$$T = \frac{t}{n_{\nu}} = \frac{60}{14} = 4.286 \, s \tag{1}$$

The angular velocity of the whole wheel ω_k is obtained by dint of formula (2):

$$\omega_k = \frac{2 \cdot \pi}{T} = \frac{2 \cdot \pi}{4.286 \, \text{s}} = 1.466 \, \text{s}^{-1}$$
 (2)

We consider the circumferential speed of the wheel v_{ok} in the vertical position, where the wheel describes the largest diameter by tilting the gondolas during riding of amusement device. Accordingly, we can determine the desired diameter and the resulting formula (3) for the circumferential speed is subsequently:

$$v_{ok} = \frac{D_{ck}}{2} \cdot \omega_k = \frac{13,66 \, m}{2} \cdot 1,466 \, s^{-1},$$

$$v_{ok} = 10,015 \, m \cdot s^{-1}$$
(3)

The angular acceleration of the wheel ε is obtained by the dividing angular velocity ω_k by the starting time t_r according to equation (4):

$$\varepsilon = \frac{\omega_k}{t_r} = \frac{1.466 \, s^{-1}}{17 \, s} = 0.086 \, s^{-2} \tag{4}$$

The circumferential speed of passengers v_{op} is measured 0.6 m from the seat surface, and it is calculated based on formula (5), where D_{pk} is wheel

diameter measured between two opposite gondolas at the passenger seat:

$$v_{Op} = \frac{D_{pk}}{2} \cdot \omega_k,$$

$$v_{Op} = \frac{11.214 \, m}{2} \cdot 1.466 \, s^{-1},$$

$$v_{Op} = 8.22 \, m. \, s^{-1}$$
(5)

The acceleration due to gravity acting on the passengers a_p can be calculated according to equation (6), where r_{op} is the radius of the wheel measured between two opposite gondolas at the point of the passenger seat, g is the gravitational acceleration, F_{od} is centrifugal force of the gondola and F_g is the weight of the gondola:

$$a_{p} = \frac{F_{od}}{F_{g}} = \frac{m \cdot v_{Op}^{2}}{m \cdot g} = \frac{v_{Op}^{2}}{r_{Op} \cdot g}$$

$$a_{p} = \frac{8.22^{2} \, m. \, s^{-1}}{5.61 \, m \cdot 9.81 \, m. \, s^{-2}} = 1.23g$$
(6)

The calculated gravitational acceleration is considered in the equilibrium position of the device, inasmuch as the passengers get into the position when they ride in a vertical position downwards, the gravitational acceleration of the Earth must be added. The resulting maximum gravitational acceleration acting on the passengers is $a_{p_{max}} = 2.23$ g. These physical values are suitable for a rough description of the amusement device.

When designing the principal structural elements of an amusement device, the standard prescribes a condition of permissible deflection of the structure w_{per} , which the designer must not exceed (w_{per} = L/500, valid for all structural units carrying passengers, where L (cm) is the length of the verified structure) [2]. Verifications of the structure are performed at the most adverse effects of loads on the structure [7]. Welding is used to join many components of the structure [8]. The fatigue calculation for amusement devices assumes 35 000 operating hours without considering the time of boarding and disembarking passengers. Components of regular mass production (for example, bearings, large-sized slewing bearings), which are replaced more frequently, must be rated for 5 000 hours of operation. Structural components designed with a partial safety factor $\gamma_{MF} = 1.1$ (-) or 1.0 (-) are required to be checked periodically.

All parts subjected to pressure must be designed to withstand twice the maximum working pressure without permanent deformation or failure. Loads on pistons and cylinders are designed purely with regard to axial stresses. Telescopic jacks should be dimensioned in respect of buckling and the necessary acceleration of the telescopic system at the

beginning and end of the stroke by creating a suitable reserve for increased load. In the event of a pressure line failure, the lowering speed must not exceed $1.0 \, \text{m} \cdot \text{s}^{-1}$.

The proper operation of each amusement device is superintended by a minimum of two trained employees who are familiar with every aspect of the amusement device and supervised by a supervisor. During placement and construction, the supervisor must ascertain that the ground under the facility is sufficiently firm and nothing will hamper the movement of the attraction. Prior to installation, workers ascertain that all structural units are in fully functional condition and prepared for operation. The erection procedure should be carried out in accordance with the relevant drawings and assembly instructions. After the erection of the equipment, the supervisor personally inspects the assembly by means of the construction logbook and the manufacturer's instructions. In addition, it is essential to ascertain that the equipment is stable and stands firmly in place. Each amusement handling machine must be inspected daily in accordance with the logbook, in terms of some amusement rides this inspection may be more frequently. Moreover, the inspection includes a mandatory test run in order to check mechanical systems such as brakes, driving machines. The operator during operation checks all the requirements set by the manufacturer, for example the correct occupancy of the units, the passenger restraining before the start of the ride as well as ensuring that no passenger of an illegal age or height limit is allowed on the runway. The equipment must not operate in adverse wind speeds, the operator is required to check the wind speed sensor (anemometer) and stop the operation if the wind speed exceeds 15 m·s⁻¹ [1-4]. Other values that specify the attraction will be determined in the further solution of this issue.

III. MAIN STRUCTURAL UNITS OF THE PROPOSED AMUSEMENT RIDE

The model of the amusement device (**Fig. 2**) is created in CATIA V5. The model is composed of 18 gondolas evenly distributed around the circumference of the wheel, on which 2 seats are secured. The gondolas are attached to a steel truss which is connected to each other by means of fixing profiles. The truss structure is slid onto the wheel hub and connected to it by dint of a rod with a manufactured thread.

The hub is slid onto an oversized hollow shaft and spun by means of an electric motor. The shaft is inserted into the prime beam, which is lifted to a vertical position through a hydraulic telescopic system. The hydraulic system is supplied with fluid by means of a pump with an electric motor. The hydraulic system will be equipped with metal hoses

and two-way hydraulic lock in order to prevent damage of the amusement device (e.g., when critical elements of hydraulic system would fail). The connection of wheel hub and motor unit is depicted in the **Fig. 3**.

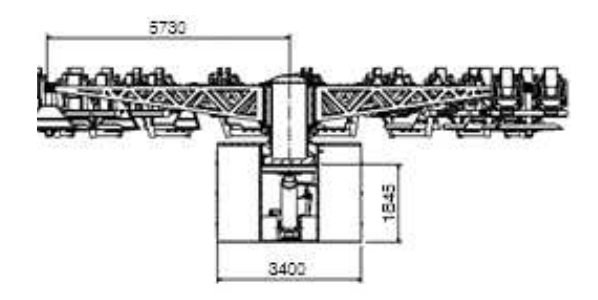


Figure 3. The wheel hub and motor unit assembly

A raised platform (podium) is built around the equipment for accessible boarding the gondola. The podium is a natural barrier from the point of view of preventing bystanders from touching the moving parts of the equipment.

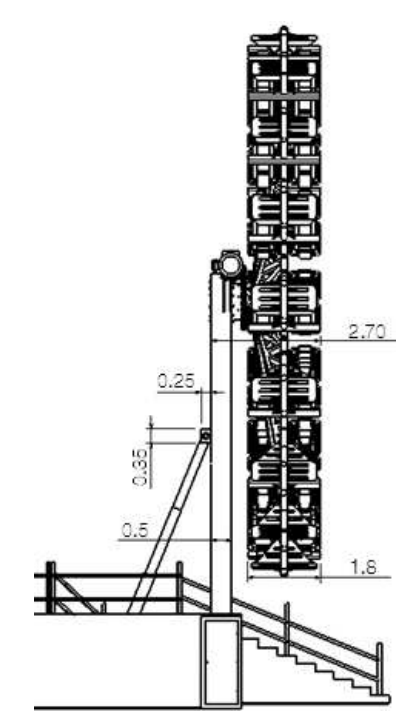


Figure 4. Main dimensions of the proposed amusement ride – side view

The entire machine covers an area of approximately 250 m^2 , the wheel diameter is 13.584 m, the overall width of the amusement ride is 15 m, the width of the wheel anchorage is 3.4 m, the width of the gondola is 1.8 m. The distance from the outside of the wheel to the outside of the beam is 2.704 m. The width of the beam is 0.5 m. The mounting of the hydraulic cylinder on the girder represents a rectangle of dimensions $0.35 \text{ m} \times 0.25 \text{ m}$. The total height from the ground is 16.870 m. The height of the equipment from the beginning of the

beam to the furthest part of the wheel is 15.325 m (**Fig. 4**) and (**Fig. 5**).

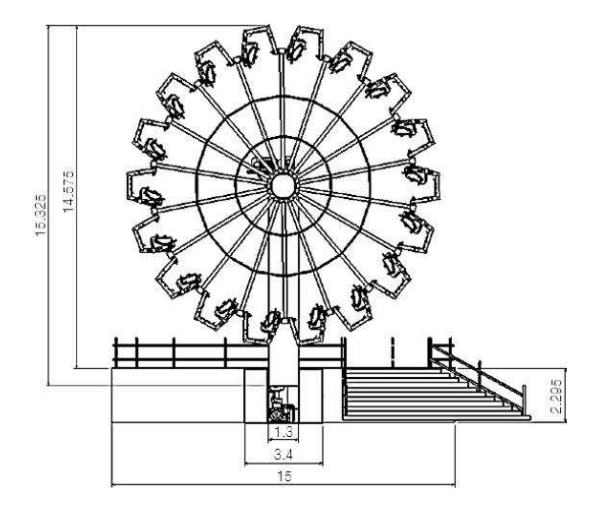


Figure 5. Chief dimensions of the proposed amusement ride – front view

The gondola shown in **Fig. 6** is designed for two passengers with a maximum load of 100 kg per passenger. The chief load-bearing parts of the gondola are constructed of structural steel. The basic load-bearing part is a tubular steel section CHS 150x5. This predominant part is welded to the beam of the SHS 150x10 (square hollow section). The seats are connected to the beam by steel sections transferring the load from the passengers to the main supporting section.



Figure 6. A 3D CAD model of the gondola

The seats are filled with foam that is covered with leather. A boarding plate is welded to the main load-bearing section. The boarding plate is employed for boarding the gondola and serves as a footrest in the course of riding. The plate is welded on rectangular profiles connected to the main supporting part of the whole gondola. A non-slip pad is glued to the boarding plate because of increasing safety when boarding the gondola.

The restraint depicted in **Fig. 7** is located behind the occupant's back and attached to the seat backrest. The restraint system comprises a restraint cage made of aluminium, which is operated by an electrical

system with a mechanical safety lock. Cage is equipped with passenger handholds due to better withstand the forces generated in the course of riding. The cage is shaped in a manner that it does not apply pressure to fragile areas when holding the passenger and provides sufficient support in the event of the passenger falling out or being ejected.



Figure 7. Restraint system of the gondola

The source of restraint system is placed in a protective box. The box is covered with metal sheets and secured against external unwanted influences. The bearing housings are fastened on the chief supporting part through 4 bolts. The housings contain single-row ball bearings (**Fig. 8**), which allow the gondola to tilt when the amusement ride is in motion. The threaded rod is pushed through the bearings, which is fixed to the truss structure and screwed with self-locking nuts. Spacer rings are

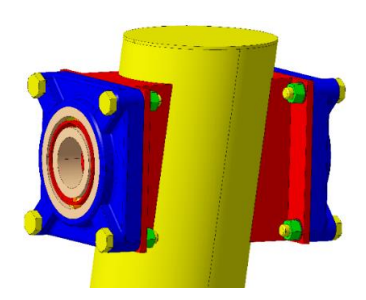


Figure 8. Gondola bearing arrangement

placed between the truss structure and the bearing because of proper function of bearings.

The truss structure (Fig. 9) is made of RHS (rectangular hollow section) 150x100x50 profile and S235 J0 material. The shape of the structure is made up of two prime members (chords). The upper member is 5.23 m long and at the end it is connected to the lower member, which is at an 8° angle to the upper member. Grips are welded on the upper member, between which the individual chords are joined together to form a single unit (wheel) by means of fixing profiles. The fixing profiles have a rectangular cross-section, where the shorter profile fastening the structure closer to the wheel mounting and the longer one fixing the truss closer to the gondola. Between the upper and lower members, the shorter members are arranged in a descending order at a 45° angle. The exceptions represent the first and

last members, which are perpendicular to the upper long member of the structure. A hole is made in the first perpendicular member into which a rod is inserted. The rod connects the truss and the wheel hub. All parts of the truss are connected by welded joints.

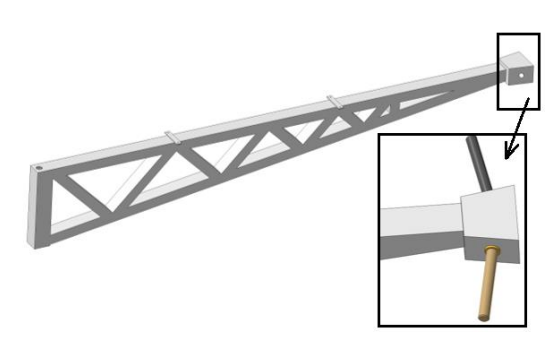


Figure 9. Truss supporting gondola

At the end of the structure is located a steel reinforcement in which the threaded rods are pressed (**Fig. 9**). The gondolas are suspended by these rods from steel reinforcement of the truss. The reinforcement is cut at a 10° angle in order that the bars are aligned on adjacent trusses, ensuring that the gondola can tilt.

The design of the truss structure, investigation of its maximum deflection and finding the most stressed member of the structure were the main objectives of the authors in the paper [21]. On the basis of the passenger body dimensions stated in STN EN 547-3 + A1, the structural design of the gondola of the amusement device (Fig. 6) was carried out, and the maximum load capacity of the gondola was determined to be 100 kg. Moreover, the restraint system of the gondola (Fig. 7) was designed with regard to ISO 17842-1:2023 standard. Subsequently, after assigning the materials, the mass of the gondola was obtained by means of Catia V5 software, approximately 705 kg. Further in the paper, the authors found and calculated the loads acting on the truss structure supporting the gondola, such as the centrifugal force of the gondola (where it was based on the calculated angular velocity of the wheel - equation (2)), the weight of the gondola, the centrifugal force of the truss structure itself. In addition, all load values had to be multiplied by the partial safety factor for variable effects, which takes values from the range (1.1 to 1.35), based on STN EN 13814-1 standard. The authors further set out to size the truss structure, based on STN EN 13814-1, which specifies the condition of maximum allowable deflection. Verification of the required deflection was performed by FEM simulation in Ansys software. Results (Fig. 10) demonstrate that the maximum deflection of the truss structure $w_{max} =$ 0.848 cm was less than the allowable deflection $w_{allowable} = 1.05 cm$ given by STN EN 13814 standard [21].

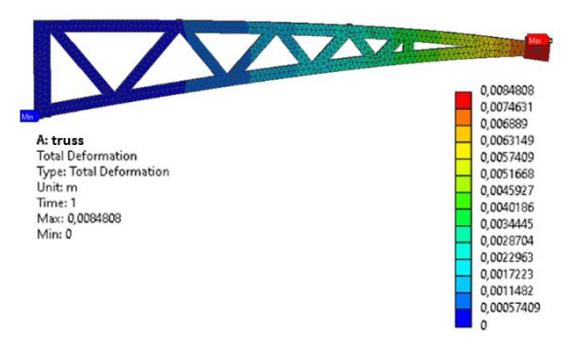


Figure 10. The total deflection of the truss [21]

The wheel structure of the amusement device is joined in the wheel hub. The hub provides the transmission of rotational motion from the motor to the wheel through the gearing. The primary component is an oversized hollow shaft fixed to the main beam of the device. A retainer is slid onto the main beam. Moreover, the holder is screwed against the shaft using eight M16 screws, which ensures that the hub is moved in the lower horizontal position of the device. The first oversized ball bearing is further slid onto the shaft. Further, the lower ring of the bearing is forced against a milled section on the shaft to ensure the bearing is functional. Before the drum is inserted, it is suggested to insert a spacer. The spacer ensures that the bearings do not move towards each other on the shaft. A shaped drum is slid onto the bearing on which the gear wheel is bolted. Flanges are welded to the drum, between which the individual trusses are inserted. After the drum has been inserted, a second bearing is embedded. A stop is made in the drum for bearing. The purpose of the stop is to prevent unwanted movement of the bearing as well as of the whole drum along the shaft. A retaining washer is screwed onto the end of the shaft for the sake of prevention of the overall movement of the second bearing out of the hub. Ultimately, a hub cover is fitted, which is screwed onto the drum. The hub cover has an oval shape and a lug by means of which is pressed against the drum as well as against the second bearing. The whole hub is made of steel and weighs approximately 5 tonnes (Fig. 11).



Figure 11. Wheel hub (top – assembled, bottom – disassembled)

The hollow shaft is inserted into the main beam 0.05 m and screwed with long M39 screws. Thus, the folded hub (**Fig. 11**) is approximately 1.5 m long. The shaft is stressed for bending in the vertical position of the device.

In the course of gear sizing, a spur gear with straight teeth (**Fig. 12**) was chosen. It can transfer a large torque from the motor to the wheel bearing due to the meagre losses. The small gear (pinion) is attached by dint of a tight key to the output shaft from the motor gearbox and secured by a washer with a bolt. The pinion turns the large gear attached to the wheel hub. The teeth on the large gear and the small pinion are designed with a modulus of m = 12 mm to withstand the high bending moment generated during the pinion and the large gear meshing. The axial distance between the gears is a = 0.792 m.

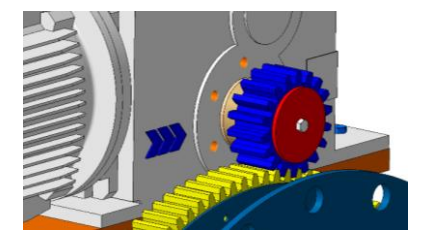


Figure 12. The designed gearing

The propulsion of the amusement device is provided by an electric motor with a bevel-front gearbox and a built-in brake (Fig. 13).

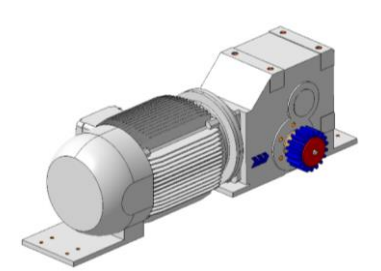


Figure 13. Electric motor with gearbox

The drive assembly is fastened on the primary beam by dint of 8 screws. The motor drives by means of the gear the wheel hub and spins the wheel to the desired speed. The change of the motor speed is ensured by selecting the frequency converter mounted at the control panel of the device. A self-powered brake is incorporated into the drive, housed at the rear of the electric motor.

The primary beam of the amusement device is made of S335 J0 steel and RHS profile (**Fig. 14**). The primary beam is fixed in the anchorage of the structure by a rod which is equipped with bearings. Therefore, this arrangement ensures a 90° change of column position. A catch is welded to the beam to which the hydraulic system is connected. The hole is manufactured at the top of the structure for the

hollow shaft to slide into. In addition, the shaft is reinforced at the hole due to allow the material to withstand the full load from the wheel. Above the hole is a notch up to approximately half the width of the beam, where a steel plate is mounted against which the motor and gearbox are bolted.

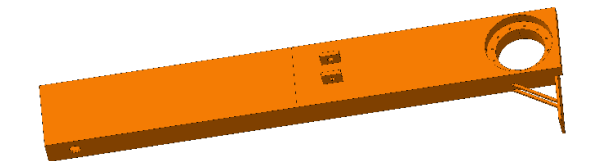


Figure 14. A primary beam of the proposed amusement ride

Another crucial element of the amusement device is the main beam. The authors aimed to scrutinise the main beam in the paper [22]. They performed sizing of the primary beam, analytical calculation as well as numerical calculation of the maximum deflection of the main beam, which must not exceed the permissible deflection given by the condition stated in STN EN 13814-1, namely $w_{per} = \frac{L}{500}$, where L is the length of the main beam. The value of the maximum permissible deflection is $w_{per} = 1.71 \ cm$. The results of the maximum deflection of the primary beam obtained from the analytical calculations ($w_{max} = 1.59 \ cm$) and FEM analysis (Fig. 15) are similar and less than the value of the permissible deflection [22].

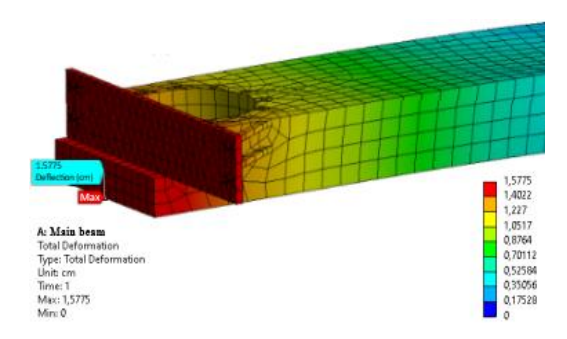


Figure 15. A detail of total deflection of main beam [22]

The hydraulic telescopic system (**Fig. 16**) is made up of 3 hydraulic cylinders. Extension occurs in the horizontal position where the system must overcome the greatest loads.

Hydraulic cylinder No. 1 starts pushing at a 50° angle over a length of 1.4 m. Hydraulic cylinder No. 2 starts pushing at a 46.88° angle over a length of 1.6 m and the last cylinder No. 3 starts pushing the beam at a 53.484° angle over a length of 1.8 m until the final position, in other words, until the beam is in the vertical position. The total extension length is 6.98 m. It is considered from the catch of the telescopic system. The hydraulic cylinders are attached at one end to mounting bracket placed at the upper part of the beam and at the other end

in the anchorage of the whole amusement device. Liquid is injected into the hydraulic system at a pressure of 35 MPa through a pump driven by the electric motor located in the anchorage of the equipment. The oil is pumped from a collection tank attached to the anchorage and located above the pumping device. The kinematics of the proposed amusement device is graphically produced in the DMU (Digital Mock-Up) Kinematics environment in CATIA V5 programme. The amusement device can be defined by 4 positions when it changes its state.

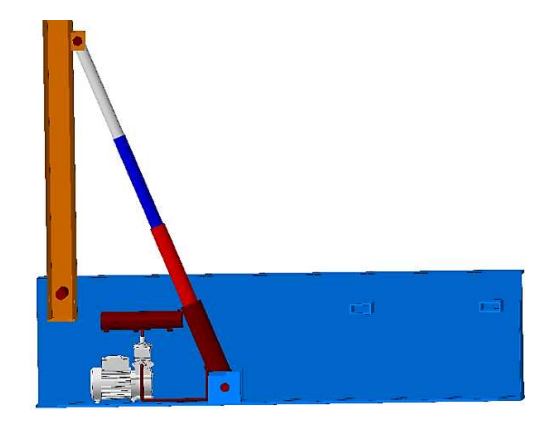


Figure 16. A side view of the telescopic system

The first position is the steady state, time for passengers to board or disembark, restraint attachment, start of the ride or end of the ride, as shown in **Fig. 17**.



Figure 17. First position of proposed amusement ride [23]

The second position occurs when the device is spun at a constant speed, before the lifting starts, when the tilting of the gondolas is observed (**Fig. 18**).



Figure 18. Second position of the amusement ride [23]

The third position is the one at which the device starts to raise or lower at the end of the ride by means of the telescopic system (Fig. 19).



Figure 19. Third position of the amusement device [23]

The last position – top, when the device reaches a vertical state, the gondolas are fully tilted, passengers ride in the upside-down position (**Fig. 20**).



Figure 20. Fourth position of the amusement device [23]

IV. CONCLUSION

The authors presented in the paper the analysis of the normative requirements necessary to perform the structural design of the handling machine serving the amusement industry. In addition, they demonstrated the technical specifications of the proposed equipment. Accordingly, they published structural designs of the diverse nodes of the mechanism and the kinematic possibilities affecting the occupants. In further research, the authors will focus on the dimensional calculations of the selected structural units by means of analytical and numerical methods.

ACKNOWLEDGEMENT

This research was supported by the Cultural and Educational Grant Agency of the Ministry of Education of the Slovak Republic in the project No. KEGA 031ŽU-4/2023: Development of key

5574

competencies of the graduate of the study program Vehicles and Engines.

AUTHOR CONTRIBUTIONS

D. Molnár: Conceptualization, Modelling, Writing, Theoretical analysis.

M. Blatnický: Conceptualization, Writing, Review and editing, Supervision.

J. Dižo: Supervision, Review and editing.

S. Solčanský: Theoretical analysis.D. Čierňava: Modelling, Writing.

REFERENCES

- [1] Safety of amusement rides and amusement devices Part 1: Design and manufacture, ISO 17842-1:2023 (2023).
- [2] Safety of amusement rides and amusement devices Part 1: Design and manufacture, STN EN 13814-1:2019 (2019).
- [3] Safety of amusement rides and amusement devices Part 2: Operation, maintenance and use, STN EN 13814-2:2019 (2019).
- [4] Safety of amusement rides and amusement devices Part 3: Requirements for inspection during design, manufacture, operation and use, STN EN 13814-1:2019 (2019).
- [5] J. Bujňák, J. Vičan, Design of steel structures, (in Slovak), EDIS, Žilina, 2012.
- [6] K. Woodcock, Human factors and use of amusement ride control interfaces, International Journal of Industrial Ergonomics, 44 (1) (2014) pp. 99-106. https://doi.org/10.1016/j.ergon.2013.08.009
- [7] M. Rhode, Loads on and strengths of amusement rides, Steel Construction: Design and Research, 11 (3) (2018) pp. 232-239. https://doi.org/10.1002/stco.201810026
- [8] R. Koňár, M. Mičian, et al., Numerical simulation of a temperature field during multibeads surface welding, Journal of Applied Mathematics and Computational Mechanics, 20 (1) (2021) pp. 49-59. https://doi.org/10.17512/jamcm.2021.1.05
- [9] H. Wen, I. Zhao, W. Chen, The Data-Driven Multivariate Process Monitoring and Diagnosis of Rides in an Amusement Park, in: Proceedings of 2018 12th IEEE International Conference on Anti-counterfeiting, Security, and Identification (ASID), Xiamen, China, 2018, pp. 136-140. https://doi.org/10.1109/ICASID.2018.8693125
- [10] A. M. Pendrill, Mathematics, measurement and experience of rotations around three axes, European Journal of Physics, 40 (1) (2018) pp. 1-14. https://doi.org/10.1088/1361-6404/aaee22

DISCLOSURE STATEMENT

The authors declare that they have no known competing financial interests or personal relationships that could have appeared to influence the work reported in this paper.

ORCID

- [11] P. Stenzler, H. Handley, K. Woodcock, Identifying Human Factors Mismatches in Amusement Ride Containment Failure, in: P. Salmon, A. C. Macquet (Eds.), Proceedings of the Advances in Human Factors in Sports and Outdoor Recreation 2016 International Conference on Human Factors in Sports and Outdoor Recreation, Walt Disney World ®, Florida, USA, 2016, pp. 177-187. https://doi.org/10.1007/978-3-319-41953-4 16
- [12] K. Woodcock, Determining participation eligibility for amusement attractions. Procedia Manufacturing, 3 (2015) pp. 5389-5396. https://doi.org/10.1016/j.promfg.2015.07.654
- [13] K. Woodcock, Safety evaluation of amusement rides using accumulated accident data: Accident data framework, Journal of Themed Experience and Attractions Studies (JTEAS), 2 (1) (2022) pp. 40-53.
- [14] K. Woodcock, Model of safety inspection, Safety Science, 62 (2014) pp. 145-156. https://doi.org/10.1016/j.ssci.2013.08.021
- [15] B. Avery, D. R. Dickson, Insight into amusement park ride and device safety in the United States, Worldwide Hospitality and Tourism Themes, 2 (3) (2010) pp. 299-315. https://doi.org/10.1108/17554211011052221
- [16] A. M. Pendrill, D. Eager, Velocity, acceleration, jerk, snap and vibration: forces in our bodies during a roller coaster ride, Physics Education, 55 (2020) pp. 1-13. https://doi.org/10.1088/1361-6552/aba732
- [17] J. Zhang, G. Shen et al., Investigation on Acoustic Emission Characteristics of Steel Structure of Amusement Device, in: G. Shen, J. Zhang, Z. Wu (Eds.), Advances in Acoustic Emission Technology Proceedings of the World Conference on Acoustic Emission-2017, Xi'an, China, 2017, pp. 259-268. https://doi.org/10.1007/978-3-030-12111-2_24
- [18] J. Harušinec, A. Suchánek et al., Design of a prototype frame of an electrically driven three-

- wheel vehicle, MATEC Web of Conferences, 254 (2019) pp. 1-9.
- https://doi.org/10.1051/matecconf/2019254020
- [19] M. Blatnický, J. Dižo et al., FEM analysis of main parts of a manipulator for mounting a compressor to a car equipped with a pneumatic suspension system, Diagnostyka, 21 (2) (2020) pp. 87-94.
 - https://doi.org/10.29354/diag/122549
- [20] Safety of machinery. Human body measurements Part 3: Anthropometric data, STN EN 547-3+A1, (2009).
- [21] M. Blatnický, D. Molnár et al., Design and Sizing of Structural Units of Technical Equipment Working in the Amusement Industry, Lecture Notes in Networks and Systems, 807 (2023) pp. 255-268. https://doi.org/10.1007/978-3-031-46874-2 23
- [22] D. Molnár, V. Ishchuk et al., Dimensional calculation of the main beam of a technical equipment intended for the amusement industry, in: M. Rackov, R. Mitrović, M. Čavić (Eds.), The 12th International Conference KOD 2024 Machine and Industrial Design in Mechanical Engineering: KOD 2024, Hotel Marina, Balatonfüred, Hungary, 2024, in review.
- [23] M. Blatnický, J. Dižo et al., Analysis of normative requirements and technical specifications in the design of handling equipment for the amusement industry, in: P. Zimniak (Ed.), XIX International Technical Systems Degradation Conference: TSD 2022, Armed Forces Academy of general Milan Rastislav Štefánik, Liptovský Mikuláš, 2022, pp. 25-28.



This article is an open access article distributed under the terms and conditions of the Creative Commons Attribution NonCommercial (CC BY-NC 4.0) license.

AJ

ACTA TECHNICA JAURINENSIS

Vol. 17, No. 2, pp. 75-83, 2024 10.14513/actatechjaur.00736



Research Article

Tool path planning of ball-end milling of free-form surfaces as a search algorithm

Abdulwahab Mgherony¹, Balázs Mikó^{1,*}

¹Institute of Mechanical engineering and Technology, Óbuda University Népszínház u. 8, 1081 Budapest, Hungary *e-mail: miko.balazs@bgk.uni-obuda.hu

Abstract:

This paper introduces an innovative approach for generating three-axis CNC tool paths for machining free-form surfaces. The method is designed to minimize variations in the effective tool diameter, addressing a common challenge encountered when using ball-end tools for machining free-form surfaces. These surfaces exhibit varying inclinations, leading to fluctuations in the tool's working diameter from one point to another, resulting in inconsistent cutting speeds and milling parameters despite a constant spindle speed. Consequently, the machined surface tends to lack uniformity. In contrast to conventional tool path planning techniques, the proposed method calculates the working diameter at each adjacent point and guides the tool's movement towards the point where the smallest change in working diameter is anticipated. This approach reduces fluctuations in cutting speed and promotes the generation of a more homogeneous surface.

Keywords: Working diameter; Ball-end tool; Free-form surface; Surface roughness; Three-axis milling

I. Introduction

The productivity of the milling process of the free form surfaces is determined by the machining circumstances, like the cutting tool properties, the cutting parameters, and the applied tool path strategy. The parameters of the milling process affect the micro- and macro accuracy of the machined surface. In order to improve the machining performances, there are several ways to optimize the technology and reduce the cost of the production.

The term "tool path" denotes the specific trajectory along which a machine's cutting tool moves to shape the desired surfaces [1]. Typically, Computer-Aided Manufacturing (CAM) systems are employed to generate this tool path for guiding CNC machines. This process gains even greater significance in the context of machining free-form surfaces, which have become increasingly prevalent across various industries like die and mould manufacturing, automotive aerospace, and production. Consequently, the automated generation of tool paths has assumed paramount importance since surface quality and machining efficiency hinge on the chosen tool path [2]. Various tool path planning strategies exist, including the iso-parametric line method, iso-scallop method, and iso-metric section plane method, among others [3]. However, these methods often lack clear guidance for selecting the optimal strategy. Thus, users are compelled to rely on a trial-and-error approach, which not only consumes time but is also suboptimal and prone to errors [4].

Hence, the paramount importance lies in devising an efficient and adaptable intelligent method for the individualized generation of tool paths customized to each specific surface. Nevertheless, the development of such a system presents a formidable challenge owing to the multifaceted variables influencing the machining of free-form surfaces, encompassing factors such as surface inclination, cutting speed, and various cutting parameters. This underscores the imperative for an advanced tool path planning approach capable of effectively addressing these intricate parameters to enhance surface quality and machining efficiency.

Many studies in this field primarily focus on optimizing cutting conditions through suitable milling strategies. While these approaches work well for machining numerous parts, they face challenges in achieving satisfactory surface quality on complex surfaces. For instance, J. Varga et al. [5] conducted a comparative study on four milling strategies using a ball-end tool and found that the constant Z strategy minimized shape deviations, resulting in an unoriented surface. D.-D. Vu et al. [6] optimized tool paths for sculpted surfaces during three-axis end

milling, reducing tool path length by 20% compared to conventional methods. G. Huo et al. [7] introduced an innovative approach for generating tool paths for free-form surfaces using a three-axis machine, ensuring alignment with desired feed directions across the entire surface.

Additionally, A. Mali et al. [8] explored the influence of cutting parameters and tool-path strategies on tool wear, cutting forces, and surface quality when milling curved surfaces, emphasizing the importance of factors like cutter diameter, and cutting speed.

In a different approach, A. Kukreja and S. S. Pande [9] developed a machine learning system that selects the best toolpath planning strategy for CNC machining complex surfaces using performance parameters and a Convolutional Neural Network (CNN), achieving 96.8% accuracy. Simultaneously, U. Župerl et al. [10] presented a cloud-based system for real-time tool condition monitoring during end milling, employing IoT, an optical system, and AI to detect cutting chip size and analyse cutting force trends, achieving 85.3% accuracy in identifying tool breakage.

Furthermore, J. Zhang et al. [11] developed an optimization model to plan tool paths, aiming to minimize path length while considering tolerance and complete milling constraints. In the study by Kukreja and S. Pande, [12], an optimized tool path was introduced utilizing the iso-scallop approach. Furthermore, the algorithm in the research offers two distinct strategies: iso-scallop and hybrid isoscallop. This methodology involves the stitching and refinement of overlapping toolpaths. Meanwhile, in the study by Liu et al. [13] a highly efficient method for generating iso-scallop tool paths was presented. This method directly computes scallop points and cutter location (CL) points for iso-scallop paths from scattered data points using iterative algorithms, eliminating the need for point offsetting surface fitting. Remarkably, this new approach has showcased superior efficiency when compared to their previous method [14]. These distinct researches endeavours collectively contribute to advancing tool path optimization and machining efficiency.

Tool path optimization has several aspects, and effects. These can be the reduction of the tool load, improvement of the surface roughness, avoidance of the burr or incensement of the dynamics of the feed.

The aim of our research is to optimize the milling tool path of the ball end milling based on the calculation of the working (or effective, D_{eff}) diameter. In the case of free form milling, the working diameter is changed because of the changing of the surface inclination. The changing working diameter has an effect on the cutting speed and the surface roughness. During the previous research stage, these effects were investigated, and

an optimization algorithm was developed, which modified the spindle speed and the feed in order to compensate the negative effect of the working diameter. The algorithm requires the tool position data and the surface inclination. The APT file format is used for tool path and the STL format for surface description. The modified NC code contains the variable cutting parameters. The acceleration and the breaking of the spindle depending on the surface inclination, and the dynamic load of the spindle, can be high [15].

In the current article, a new concept is presented, when the tool path is modified based on the changing of the working diameter of the ball-end tool.

II. THE CONCEPT

The algorithm has been developed with a specific focus: generating an optimal tool path for milling free-form surfaces. The primary objective is to minimize variations in the working diameter of the ball-end tool during the machining process. By achieving minimal changes in the working diameter, the resulting reduction in cutting speed fluctuations ensures a more uniform and homogeneous machined surface.

The core objective of the algorithm is to perform path planning for CNC machining. This involves determining the sequence of points (toolpath) that the CNC machine should follow while milling the freeform surfaces. The developed algorithm solves the tool path re-planning as a search algorithm. The algorithm uses the pre-generated NC code in APT form. The code contains the points of the toolpath. The search algorithm reorder the points in order to equalize the value of the working diameter, and reduce the dynamic load of the spindle. The algorithm implements a path planning that takes into account the difference in the effective diameter between the current point and its neighbour points. Once a point is processed, it is marked as visited (tabu) to prevent the algorithm from revisiting it. The overarching goal is to ensure that the algorithm systematically covers all points without duplication while minimizing fluctuations in the working diameter.

The algorithm begins by reading and processing data from an STL file, which represents 3D models using triangular facets and contains vital geometry information. Subsequently, it extracts tool position coordinates from an APT file, a format used in CNC machining. To enhance precision, the code generates additional tool positions as needed and calculates normal vectors at each position based on facet data from the STL file. It also determines neighbour points and computes the working diameter using an established mathematical model. Finally, the code's core objective is path planning for CNC machining, aiming to optimize toolpaths by considering

variations in the effective diameter while efficiently covering all points on the surface.

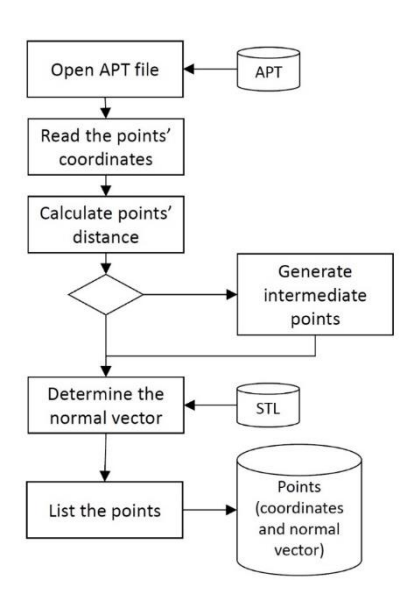


Figure 1. Pre-processing of the tool position and surface data.

Fig. 1 shows the pre-processing of the tool path and the surface data. The algorithm can be summarized in the following sequential steps.

The developed algorithm uses APT file to determine the tool position coordinates at each point of the surface. An APT (Automatically Programmed Tool) file is a file format used in computer-aided manufacturing (CAM) and computer numerical control (CNC) machining. APT is a high-level programming language specifically designed for defining toolpaths and machining operations for CNC machines. By reading the file, the algorithm extracts tool position coordinates.

The original CNC code contains the points of the tool path. The distance of the consecutive points depends on the surface inclination. In the case of plane surface segments, which can be horizontal or inclined, the distances can be large. But where the curvature of the surface is greater, the distance between the points is smaller. In order to reconfigure the tool path, quasi-equal density of the points is required. If the distance of points is larger than the defined limit (d_{lim}) , new points are added. The suggested limit is the value of the width of cut parameter (a_e) , which is the distance between two parallel paths. The procedure divides the line between two points into pieces, where the distance is smaller than the defined limit. It has no effect on the accuracy of the machining because the original tool path follows the same linear segment.

The distance between two points is:

$$\mathbf{d_i} = \tag{1}$$

$$d_{i} = (1)$$

$$\sqrt{(x_{i} - x_{i+1})^{2} + (y_{i} - y_{i+1})^{2} + (z_{i} - z_{i+1})^{2}}$$

$$I = Roundup\left(\frac{d_{i}}{d_{lim}}\right) (2)$$

If I > I, additional points must be added, the number of new points is (I-1). The coordinates of the new points can be calculated by the next equation:

$$\underline{P}_{\text{new}_{j}} = \underline{P}_{i} + \frac{j}{I} \cdot \left(\underline{P}_{i+1} - \underline{P}_{i}\right) = \begin{bmatrix} x_{i} + \frac{j}{I} \cdot (x_{i+1} - x_{i}) \\ y_{i} + \frac{j}{I} \cdot (y_{i+1} - y_{i}) \\ z_{i} + \frac{j}{I} \cdot (z_{i+1} - z_{i}) \end{bmatrix};$$

$$j = 1 \dots (I - 1) \tag{3}$$

The algorithm proceeds by processing data from the STL file, which is commonly used for representing 3D models with triangular facets. STL file contains information that characterizes the surface's geometry. This file format presents the surface as a collection of triangles along with their associated normal vectors within a threedimensional coordinate system. It's important to note that the STL file does not contain any additional surface details, such as colour or texture information. As the algorithm reads the STL file, it accumulates a list of the normal vectors, and calculates the in-center point of each triangle (Fig. 2). The resolution of the STL file can be adjusted. The STL file describes the free form surface with some deviation, but this has no effect on the accuracy of the method, because only the normal vector of the machined area is required, and in case of technical free form surfaces, the changing is limited.

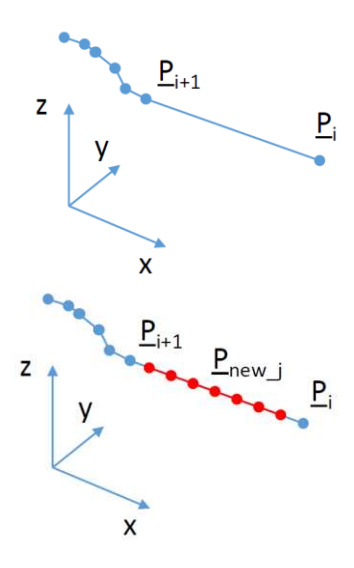


Figure 2. Intermediate points.

The algorithm calculates the normal vectors at each tool position using the facet normal obtained from the STL file. These normal vectors are associated with the corresponding tool positions by identifying the nearest in-center point. Essentially, this process ensures that at each position, the tool aligns with a specific triangle and adopts the same normal vector as that triangle.

The search algorithm of the reordering the points of the tool path is started by the selection of the starting point (Fig. 3). It has to be on the border of the machined surface. The point can be defined by rules, like the lowest or the highest point of the contour or it can be a random point.

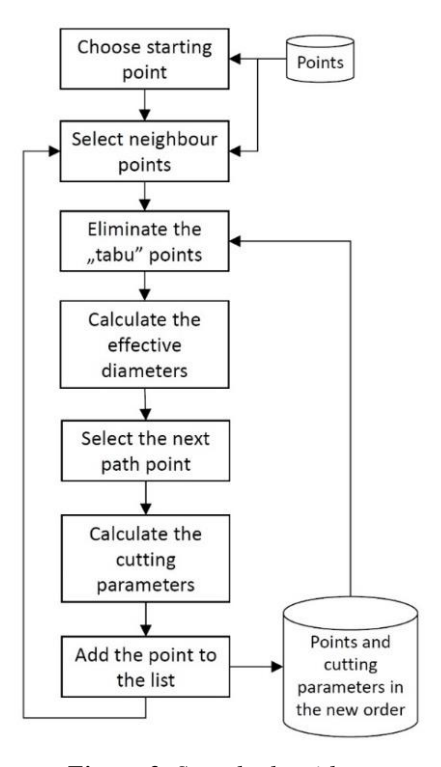


Figure 3. Search algorithm.

The next step is finding the neighbour points. Because of the non-uniform and non-regular distribution of the tool points, an adaptive method has to be used. This code then performs some neighbour point calculations based on a distance threshold R. It iterates over tool position elements and checks for nearby points. If the count of nearby points is less than a specific number, it incrementally increases the distance threshold R until it reaches or exceeds specific number of points. The resulting points are stored in a list. If a point was chosen previously, it is deleted from the neighbour set, as a tabu point.

The algorithm calculates the milling direction for each tool position based on the slopes between the tool position and its neighbour points. Then it calculates the working diameter of each neighbour point using a mathematical model presented by Mikó and Zentay [16].

At the last step, the point is selected, which has the smallest difference value in the working diameter. If there is no difference in the working diameter, because the surface is horizontal, the next point is selected in the feed direction. The modified cutting parameters (cutting speed and feed) are calculated, and add to the list of the points of the new tool path. The algorithm starts again by the selection of the neighbour points. The reordering of the points of the tool path is ended, when all points are selected.

III. RESULTS

The algorithm was tested on a free form surface (Fig. 4), the size of the part was 50×50 mm, the

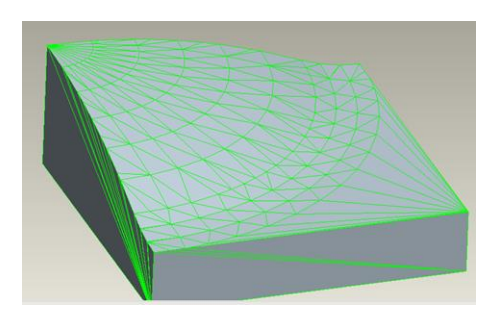


Figure 4. Test part geometry.

Table 1. Parameters of the simulation.

Parameter	Value
Tool diameter (D)	10 mm
Cutting speed (v _c)	63 m/min
Feed (v _f)	500 mm/min
Depth of cut (a _p)	0.3 mm
Width of cut (a _e)	0.5 mm
Feed direction (A _f)	90°

height of the profile was 10 mm. The machining parameter in the simulation is shown in **Table 1**.

Fig. 5 illustrates the outcome of point processing. The first image displays the original distribution of path points, while the second reveals the extended point cloud. This extension of the point cloud provides valuable data for optimizing tool paths. Algorithms can leverage this data to determine the most efficient and safe routes for the cutting tool. To maintain relatively uniform point spacing, the width of cut (ae) was used as a standard distance between points. This approach ensures reasonably consistent inter-point distances. Moreover, extending the original point cloud allows for a faithful representation of the complex free-form surface geometry, thereby enhancing the precision of tool path planning and reducing the risk of errors or defects in the final product.

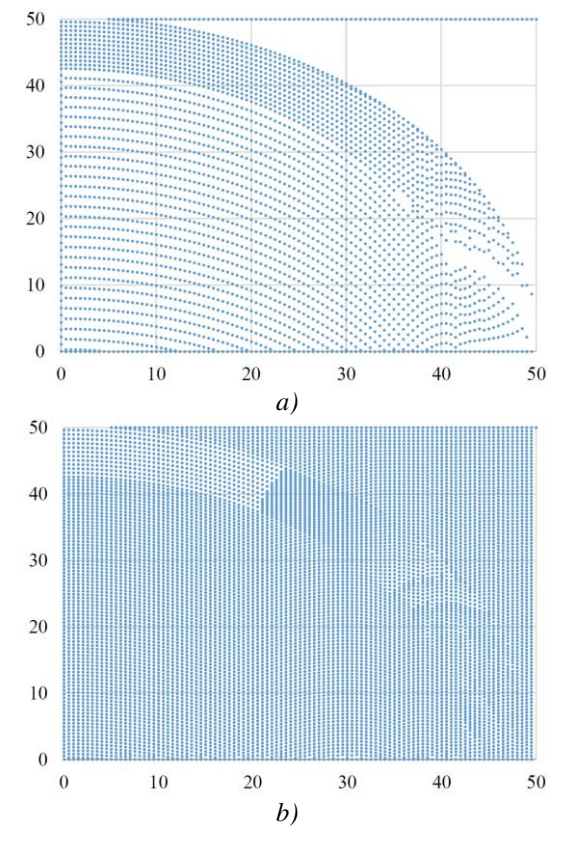


Figure 5. (a) Original and (b) extended distribution of the points.

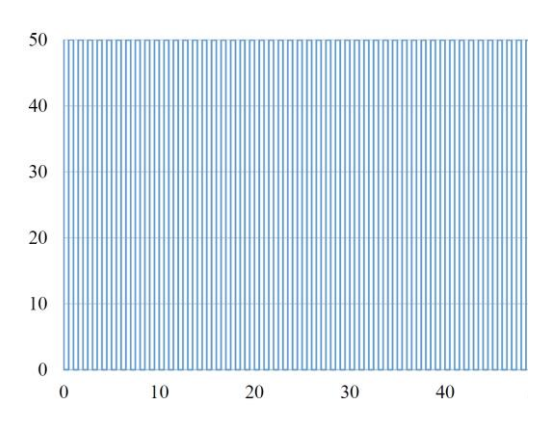


Figure 6. Original tool path.

In **Fig. 6 and 7**, a tool path comparison between the original and optimized versions is presented. The optimized tool path originates from two positions: the point with index 0, coordinates 50, 50, 10 (located in the top right corner of the workpiece), and the point with index 4269, coordinates 28.500, 43.919, 10.00 (situated in the middle of the workpiece). The optimization considers both 4 and 8 neighbour points.

It is important to note that the generated path contains jump points. These occur when all adjacent points to the current position are marked as visited. In such instances, the algorithm seeks the closest unvisited point in the tool-position list. However, this optimization strategy involves a trade-off; the

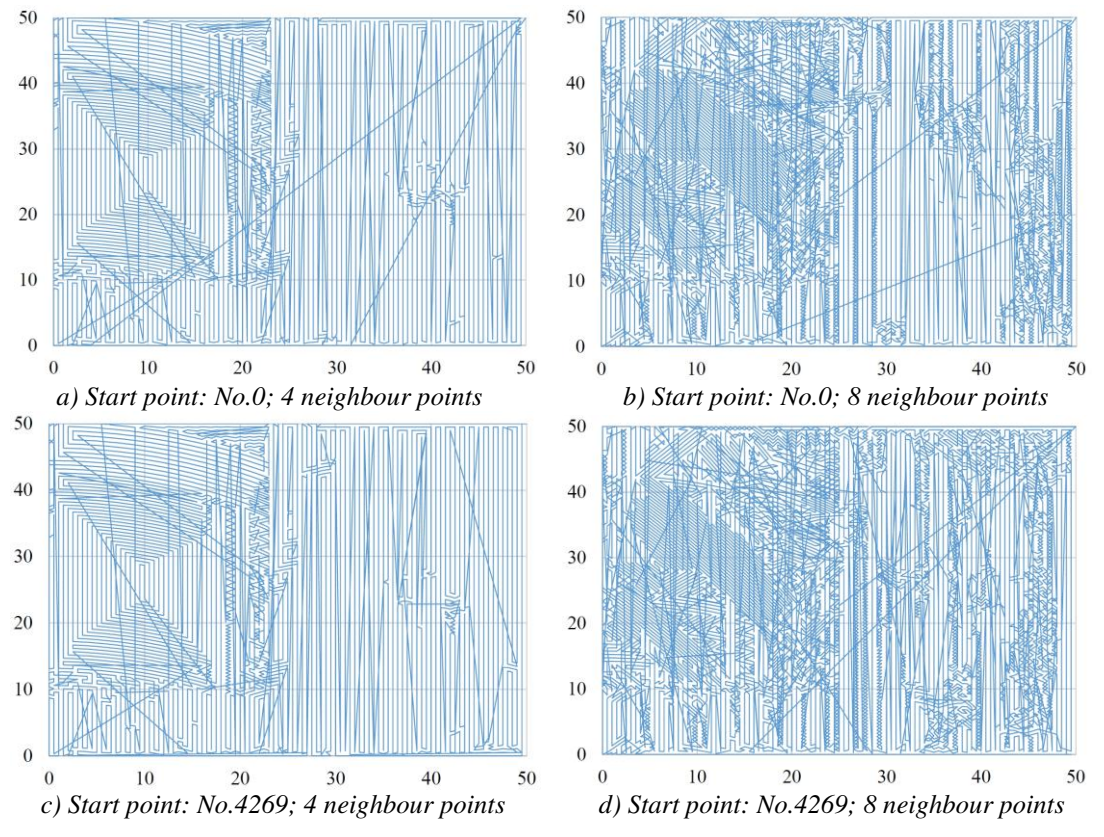


Figure 7. Optimized tool path.

tool may traverse a greater distance in the optimized path compared to the original path.

The result of the optimized toolpath depends on the position of the starting point, and the number of the investigated neighbour points. Therefore, four cases were studied (**Table 2**).

The comparison of the four tool path planning cases unveils distinct trends influenced by the selected starting points and the number of neighbouring points. **Fig. 8a** illustrates the traveling distance in the four cases. Cases 1 and 3, both originating from the top right corner but differing in neighbouring points, demonstrating that an increase in neighbouring points leads to a longer tool path (6183) for Case 1 with four neighbours and 8805 for Case 3 with eight neighbours. Similarly, Cases 2 and 4, both starting from the middle but varying in neighbouring points, follow a similar pattern, with Case 4 (10645) having a longer tool path compared to Case 2 (7097). Conversely, **Fig. 8b** highlights the impact of starting points and neighbouring points on

Table 2. Parameters of the simulation.

Case	Starting point	Neighbours
1	0	4
2	4948	4
3	0	8
4	4948	8

jumping points. Initially comparing Cases 1 and 2, both starting from distinct locations but with four neighbouring points, reveals a minimal difference in jumping points (181 in Case 1 and 180 in Case 2). This suggests that the starting point's influence on jumping points is relatively limited when the number of neighbouring points remains constant. A parallel trend is observed in Cases 3 and 4, where starting from the middle but with different neighbouring points results in comparable jumping points (426 in Case 3 and 432 in Case 4). This underscores that the number of neighbouring points plays a more significant role than the starting point in determining the number of jumping points.

On the other hand, the main aim of the optimization was to decrease the changing of the effective diameter and moderate the dynamic load of the spindle. This aim was measured by the sum of the absolute value of the changing of effective diameter. Two cases were compared. The first case was the result of the spindle speed optimization, without any modification of the toolpath, and the second was the tool path optimization.

Fig. 9 and 10 provide a visual representation of the change in the working diameter when employing two different milling strategies: the traditional zigzag milling tool path and an optimized tool path. The working diameter, a critical parameter in machining operations, is analysed to understand its variation and impact on the machining process.

In the case of the traditional zig-zag milling tool path, **Fig. 9** illustrates a significant range of change in the working diameter, spanning from 0 to 0.9155. This wide variation suggests that the machining process under traditional zig-zag milling conditions results in a less consistent effective diameter throughout the operation.

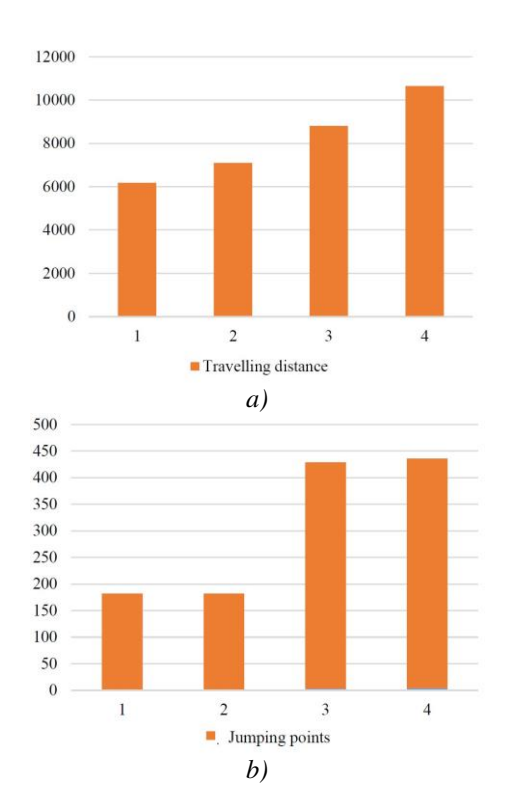


Figure 8 a) Travelling distance and b) Number of jumping points at each case.

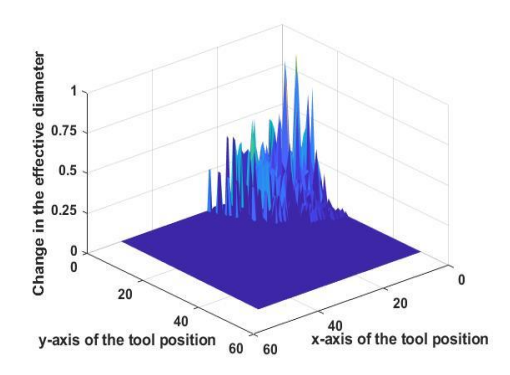


Figure 9. The change in the working diameter in the case of original tool path.

On the other hand, **Fig. 10** showcases the working diameter variation when utilizing an optimized tool path. In this scenario, the effective diameter fluctuates within a narrower range, specifically between 0 and 0.6. This narrower range indicates that the optimized tool path leads to a more controlled and predictable working diameter during the milling process.

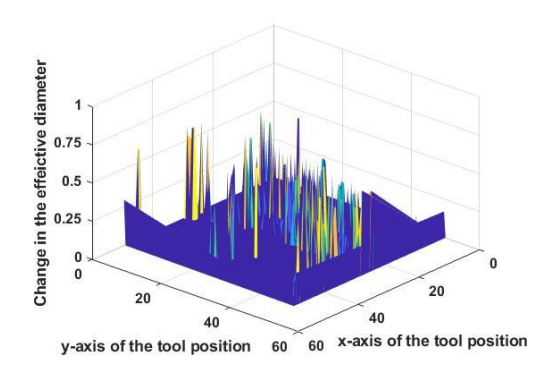


Figure 10. The change in the working diameter in the case of optimized tool path.

The observed difference in the effective diameter range between the two milling strategies has noteworthy implications, particularly in terms of surface homogeneity. A smaller variation in the working diameter, as achieved with the optimized tool path, contributes to enhanced surface homogeneity.

Fig. 11 illustrates the spindle speed change in the case of the traditional zig-zag milling approach, showcasing a wide range from 0 to 622. This broad variation implies that under traditional zig-zag milling conditions, the spindle speed undergoes significant changes throughout the machining process. Such fluctuations may introduce challenges such as tool wear, vibration, and inconsistent cutting conditions, potentially impacting the overall quality of the machined surface.

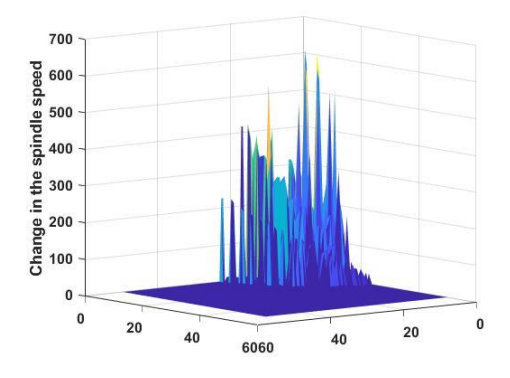


Figure 11. The change in the spindle speed in the case of original tool path

Conversely, **Fig. 12** represents the spindle speed variation for the optimized tool path. In this case, the spindle speed changes within a smaller range, specifically from 0 to 128. The narrower variation indicates that the optimized tool path leads to a more controlled and stable adjustment of spindle speed during machining.

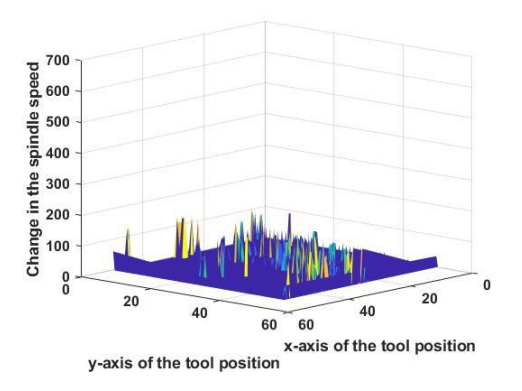


Figure 12. The change in the spindle speed in the case of optimized tool path

IV. CONCLUSION

The article presents a new concept for milling tool path optimization, when the tool path is modified based on the changing of the working diameter of the ball-end tool.

The presented algorithm was designed for optimizing toolpaths in CNC machining, with a primary focus on minimizing variations in the working diameter of the ball-end tool during milling of free-form surfaces. The algorithm reorders the tool points of the CNC program, and it works as a searching algorithm. It systematically calculates the working diameter of neighbour points and directs tool movement to points with minimal diameter differences, ensuring minimal changing of the working diameter and the changing of the spindle speed in order to maintain the constant cutting speed.

Key steps involve reading and processing data from an STL file to extract surface geometry and tool position data from an APT file. Normal vectors are calculated and associated with tool positions, aligning the tool with specific triangles of the STL file.

Neighbour point calculations consider a distance threshold, and working diameters are determined for each point. The core path planning algorithm minimizes working diameter fluctuations, preventing point revisits for efficiency.

The comparative analysis between the original and optimized tool paths highlighted the nuanced impact of starting points and neighbouring points on the resultant tool path. Successfully achieving the primary optimization goal - reducing the change in

effective diameter and moderating spindle dynamic loads - was evidenced in the controlled working diameter variation observed in the optimized tool path, contributing to enhanced surface homogeneity compared to traditional zig-zag milling, from the viewpoint of the variation of the surface roughness. From the aesthetic aspect, the surface will not homogenous, because of the non-regular tool path.

AUTHOR CONTRIBUTIONS

Mgherony A.: Conceptualization, Implementation, Testing, Writing, Data visualization.

REFERENCES

- [1] Q. Zou, J. Zhang, B. Deng, and J. Zhao, Isolevel tool path planning for free-form surfaces. Computer-Aided Design 53 (2014) pp.117–125.
 - https://doi.org//10.1016/j.cad.2014.04.006
- [2] L. C. Magalhães and J. C. E. Ferreira, Assessment of tool path strategies for milling complex surfaces in hardened H13 steel. Proceedings of the Institution of Mechanical Engineers, Part B: Journal of Engineering Manufacture 233 (3) (2019) pp. 834–849. https://doi.org// 10.1177/0954405418755824
- [3] X. Niu, T. Wang, B. Shen, T. Zhao, and Q. Huang, Study on Tool Path Optimization in Multi-axis NC Machining. MATEC Web of Conferences 34 (2015) 02012. https://doi.org//10.1051/matecconf/201534020 12.
- [4] Y. Sun, J. Jia, J. Xu, M. Chen, and J. Niu, Path, feedrate and trajectory planning for free-form surface machining: A state-of-the-art review. Chinese Journal of Aeronautics 35 (8) (2022) pp. 12–29. https://doi.org//10.1016/j.cja.2021.06.011
- [5] J. Varga, T. Tóth, Ľ. Kaščák, and E. Spišák, The Effect of the Machining Strategy on the Surface Accuracy When Milling with a Ball End Cutting Tool of the Aluminum Alloy AlCu4Mg. Applied Sciences 12 (20) (2022) 10638.
 - https://doi.org//10.3390/app122010638
- [6] D.-D. Vu, F. Monies, and W. Rubio, A new optimization tool path planning for 3-axis end milling of free-form surfaces based on efficient machining intervals. AIP Conference Proceedings (2018) 070011. https://doi.org//10.1063/1.5034907.
- [7] G. Huo et al., CNC Tool Path Generation for Freeform Surface Machining Based on Preferred Feed Direction Field. International Journal of Precision Engineering and Manufacturing 20 (5) (2019) pp. 777–790. https://doi.org//10.1007/s12541-019-00084-2.
- [8] R. A. Mali, R. Aiswaresh, and T. V. K. Gupta, The influence of tool-path strategies and

Mikó B.: Writing, Review and editing. Supervision.

DISCLOSURE STATEMENT

The authors declare that they have no known competing financial interests or personal relationships that could have appeared to influence the work reported in this paper.

ORCID

Mgherony A. http://orcid.org/0009-0001-4590-3057
Mikó B. http://orcid.org/0000-0003-3609-0290

- cutting parameters on cutting forces, tool wear and surface quality in finish milling of Aluminium 7075 curved surface. The International Journal of Advanced Manufacturing Technology 108 (1-2) (2020) pp. 589–601. https://doi.org//10.1007/s00170-020-05414-7.
- [9] A. Kukreja and S. S. Pande, Optimal toolpath planning strategy prediction using machine learning technique. Engineering Applications of Artificial Intelligence 123 (2023) 106464. https://doi.org//10.1016/j.engappai.2023.1064
- [10] U. Župerl, K. Stepien, G. Munđar, and M. Kovačič, A Cloud-Based System for the Optical Monitoring of Tool Conditions during Milling through the Detection of Chip Surface Size and Identification of Cutting Force Trends. Processes 10 (4) (2022) p. 671. https://doi.org//10.3390/pr10040671
- [11] J. Zhang, R. Mo, N. Wan, and C. Xia, Tool path planning for five-axis flank milling of free-form surfaces. The International Journal of Advanced Manufacturing Technology 108 (1-2) (2020) pp. 73–90. https://doi.org//10.1007/s00170-020-05283-0
- [12] A. Kukreja and S. S. Pande, "An Efficient Iso-Scallop Toolpath Planning Strategy Using Voxel-Based Computer Aided Design Model," Journal of Computing and Information Science in Engineering 23 (3) (2023) 031009. https://doi.org//10.1115/1.4055372
- [13] W. Liu, S.-M. Zhu, T. Huang, and C. Zhou, An efficient iso-scallop tool path generation method for three-axis scattered point cloud machining. The International Journal of Advanced Manufacturing Technology 107 (7-8) (2020) pp. 3471–3483. https://doi.org//10.1007/s00170-020-05188-y
- [14] W. Liu, L. Zhou, and L. An, Constant scallopheight tool path generation for three-axis discrete data points machining. The International Journal of Advanced Manufacturing Technology 63 (1-4) (2012) pp. 137–146.

https://doi.org//10.1007/s00170-011-3892-3

[15] A. Mgherony and B. Mikó, "Controlling the Spindle Speed when Milling Free-Form Surfaces using Ball-End Milling Cutter," Acta Polytechnica Hungarica 20 (6) (2023) pp. 135–149.

https://doi.org//10.12700/APH.20.6.2023.6.8

[16] B. Mikó and P. Zentay, A geometric approach of working tool diameter in 3-axis ball-end milling. The International Journal of Advanced Manufacturing Technology 104 (1-4) (2019) pp. 1497–1507.

https://doi.org//10.1007/s00170-019-03968-9



This article is an open access article distributed under the terms and conditions of the Creative Commons Attribution NonCommercial (CC BY-NC 4.0) license.

ACTA TECHNICA JAURINENSIS



Vol. 17, No. 2, pp. 84-90, 2024 10.14513/actatechjaur.00738



Research Article

Effects of interior doors on the audibility of fire alarms

Ágota Zsuzsanna Mohai^{1,*}, Barbara Elek¹

¹Institute of Safety Science and Cybersecurity, Donát Bánki Faculty of Mechanical and Safety Engineering, Óbuda University, Népszínház Street 8., 1081 Budapest, Hungary *e-mail: mohai.agota@bgk.uni-obuda.hu

Abstract:

One of the most important purposes of installing fire alarm systems is to provide an alarm signal in a protected building in the event of a fire. Fire alarms are most often provided by networked audible warning devices. The signal must be easily and quickly detectable and identifiable so that the occupants inside can start to escape after the alarm has been sounded. This is apparently a simple expectation, but if you look at the efficiency of fire alarms as a whole, and the effects that determine whether an evacuation will occur in response to an alarm, the question is not so simple anymore. The authors examined the circumstances that may affect the fire alarm signals. Among these aspects, the focus of the article is on the soundproofing properties of especially the interior doors, and their effect on sound propagation. The authors hypothesised that the increase in sound insulation of certain building materials and structures has an increasingly negative effect on the audibility of fire alarm signals. The authors supported their hypothesis with a series of experiments by test the soundproofing of several interior doors in response to a fire alarm sounder, used in fire alarm systems. The paper confirms that the sound attenuation of the currently used interior doors is better than that of the previously used ones and this is a negative factor for the fire alarm audibility. The authors recommend that the soundproofing properties of interior doors should be given greater weight in the design of fire alarm systems.

Keywords: fire alarm; evacuation; fire sounder; soundproof; sound pressure; alarm audibility

I. Introduction

The first devices suitable for signalling fire were the forerunners of today's manual call points, which appeared on the streets of Berlin [1] and Boston [2] in the 1850s. Their primary purpose was, in part, to replace fire towers and rudimentary devices used to signal fire. By alarming the firefighters as quickly as possible and by intervening as early as possible, the number of fatalities and injuries can be reduced, as well as property damage (Fig. 1). From the mid-20th century, in addition to manual call points, devices developed in the series, which are capable of detecting fire without a human presence, gained an increasing role. These devices are the forerunners of today's automatic detectors, which were able to detect heat, smoke, and later flames. The main purpose of all these detection and alarm devices is to alert the occupants of a protected building as early and as clearly as possible to the fire in order to enable people to escape in time.

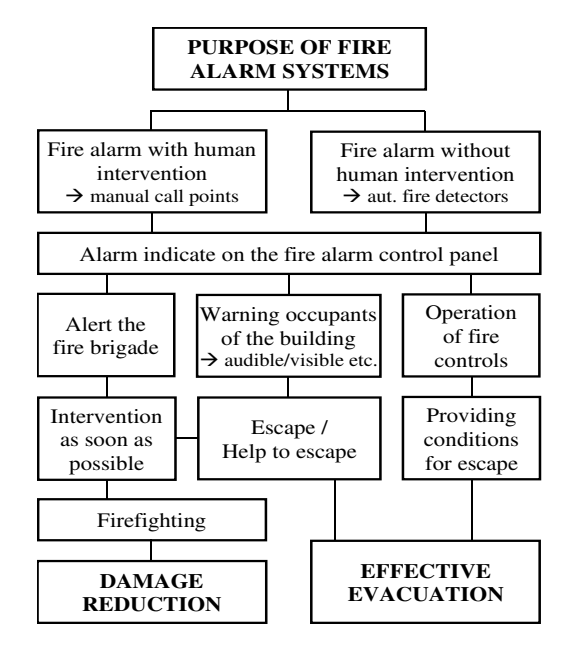


Figure 1. Purpose of fire alarm systems (source: own figure)

The key to a successful escape is the time interval (Available Safe Egress Time - ASET), which is available from the place of residence to reaching a safe area. "Defined as the time when fire-induced conditions within an occupied space or building become untenable." [3] This time is determined by calculations or simulation programs during the design phase of buildings. However, the time available for escape determined in this way is worthless if the information about the need to escape reaches the given person too late. The time from the moment of ignition to the start of escape is influenced by a number of factors (see Fig. 2).

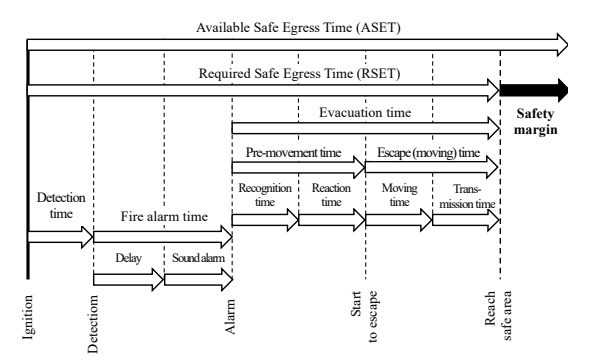


Figure 2. Evacuation elements as a function of time, Source: [13], transformed.

Each of these components can increase the time required to escape (Required Safe Egress Time - RSET) to such an extent that it reduces the chance of reaching a safe space. Therefore, the ability to effectively hear and identify the sound signal generated by the fire alarm system installed in a building at every point in the building is one of the most important components of fire safety in a building.

The design of audible fire alarm systems is subject to relatively strict standards now. Specific requirements define the minimum sound pressure level (hereinafter abbreviated as SPL) at any point of the building that the fire alarm sounders must provide. This is generally a minimum of 65 dB(A) according to the Hungarian technical specifications [4], but similar requirements are found in other countries (see **Table 1**).

At the same time, the regulations for manufacturers of fire alarm sounders also maximize the performance of sound signalling devices, taking into account the negative impact of sound on the human hearing organ above a certain sound pressure. This means that the sound pressure level, measured at a distance of one metre from the sound source, should not exceed 120 dB [5], so that the majority of fire alarm sounders on the market have a sound output rating of between 90 and 110 dB.

Table 1. Requirements of SPL in standards

Standard	Min. SPL*	Min. SPL**	Min. SPL***
TvMI 5. [4]	65	75	+5
BS 5839-1 [16]	60, 65	75	+5
NFPA72 [15]	no specific value	75	+5
DIN VDE 0833-3 [14]	65	75	+5

SPL= $sound\ pressure\ level\ in\ dB(A)$

The design of fire alarm systems has a minimum sound pressure level to be ensured and an upper limit of 120 dB, which follows from the sound pressure value that can be tolerated by the human hearing organ without damage. But there is also a third, very important aspect to consider, which is the environmental impact on sound propagation. The basis of the latter aspects is the physics of sound propagation, which depends not only on the characteristics of the sound source (primarily its frequency) but also on the particularities of the given environment. It is known that the basic physical laws mostly determine how a given sound propagates in the open air. Several methods have been developed over the past decades to determine as accurately as possible the number and location of audible warning devices, needed to meet the requirements at the design stage [6] [7] [3], however these methods show a wide variation [8].

Primarily, the distance from the sound source has a significant effect on the reduction of the sound pressure level. This can be taken into account by the easily applicable so-called '6-decibel rule', derived from the physical laws of sound propagation in free, unobstructed space. However, given that fire alarms are used in enclosed spaces, the parameters of the enclosed space are also decisive in the propagation of the sound.

Other significant influencing factors are the building structures that get in the way of the sound waves. In the context of fire alarm systems, these are walls and doors of different sizes and materials. There are 'rules of thumb' in engineering practice to take account of the sound attenuation effects of these structures, but experience increasingly shows that trends in the construction industry are prompting a rethink of the previous design practice. The sound attenuation of general building structures, including non-fire-resistant interior doors, is usually considered to be of the order of 20 dB, but our research shows that this value is often inadequate in

^{*} in common areas

^{**} to rouse sleeping people

^{***} above maximum ambient SPL of the background noise

practice. This observation is supported by a report from February 2024, which predicts a large-scale growth of the market for soundproof doors in the coming years. The report by Impulse Insight [9] says: "The increasing demand for noise reduction solutions across various sectors, including commercial, residential, and industrial, is a major factor driving market growth. The rising awareness about the importance of noise control for a comfortable and productive environment is also contributing to the market expansion."

Last but not least, the furnishings in the room and the interior coverings of the space also play a major role in the extent to which the sound is attenuated in a space of the same size and geometry.

It is not the purpose of this article to examine the conditions for fire escape in detail and in complexity, but it is worth at least reviewing what significant factors need to be taken into account in addition to ensuring adequate sound pressure levels:

- the first important condition is that the fire in the protected area is detected by the automatic detector in its early stages or that someone presses the manual call point in time;
- the signal from the alarmed detector or manual call point reaches the fire alarm control panel;
- the fire alarm control panel activates the sounders in response to the fire alarm;
- the occupant detects the audible alarm;
- identify it as a fire alarm as quickly as possible;
- and finally makes the decision to leave the location place to start the escape.

The temporal and spatial progression of this complex set of conditions is illustrated in Fig. 3.

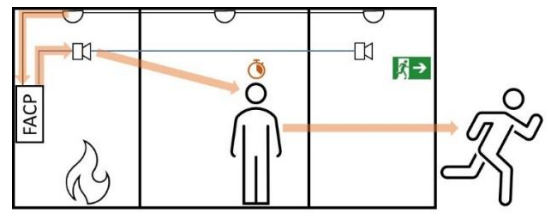


Figure 3. Components of fire escape, source: own figure

Successful escape, evacuating the occupants, is a complex problem. In addition to properly designed, implemented and operated technical solutions, one cannot forget the psychological aspect of the issue, which is both personal and social, and which is perhaps even more difficult to take into account. A fire alarm, as the 'auditory' delivery of a sound with a given frequency and pattern, by providing the appropriate sound pressure level, does not guarantee that a person will interpret this sound - as information - correctly and make the right decision to flee immediately. The human response can be influenced by a number of things, including:

- the person's skills (e.g. quick situational awareness and decision-making),
- physical and mental condition (e.g. disability),
- the knowledge he/she have or lack (e.g. whether he/she has received adequate fire safety training),
- previous experience (e.g., has he/she heard many false alarms),
- attitude (e.g. whether he or she is a rulefollowing person),
- the impact of expectations (e.g. not leaving the workplace), etc.

Among the components necessary for a successful escape, this article further investigate the issue of ensuring the sound pressure level, highlighting the interesting aspect of how doors of different materials and quality affect the propagation of fire alarm sound. The authors carried out tests, the results of which are evaluated and compared with the applied recommendations and design practices. The purpose of the paper is to draw attention to the fact that changes in the materials and solutions used in the construction industry can also affect the design practice of such a narrow and specialized field as designing fire alarm systems. The increasing soundproofing properties of interior doors is just one of many effects that affect fire alarm effectiveness. But this effect, looking at the market trend, has a large influence. "Factors such as increasing demand for noise reduction solutions, technological advancements, and regulatory requirements are driving the market growth. Manufacturers are continuously innovating and developing highperformance soundproof doors to meet the evolving needs of customers." [9]

II. THE EFFECT OF SOUND ATTACHMENT OF INTERIOR DOORS ON FIRE ALARM

To support assumptions based on the authors' experiences, sound pressure measurements were carried out of several interior doors to compare them with the 20 dB(A) equivalent used in planning the location of fire alarm sounders. The used layout of the measurement series shown in **Fig. 4**.

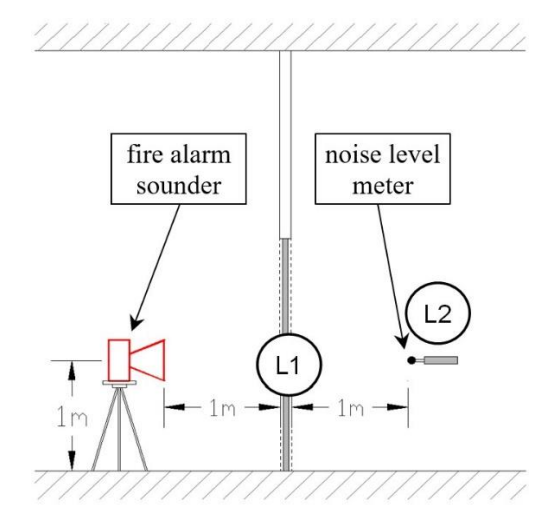


Figure 4. Examination of the soundproofing properties of interior doors in connection with the audibility of fire alarms, source: own figure

The sound pressure level differences between the two measurement points (L1 and L2) are taken as the results of the measurements.

The measurement, although similar to the measurement of airborne sound attenuation between two rooms according to the relevant standard [10], it is not the same. This measurement purposefully examined how the soundproofing effect of interior doors applies to the actual sound pressure level of the alarm sound generated by the typical sound alarm devices used in fire alarm systems.

Specifications of the fire alarm sounder device used in the measurement (**Fig. 5**) [11]:

- Type of fire alarm sounder: WES, W2-FPT-CSS;
- Manufacturer: Ramtech Electronics Limited:
- Sound output: 88-109 dB depending on the setting (in this case 100 dB according to DIP setting 6);
- Compliance with EN 54-3, EN-11, EN-25.

Technical data of the sound pressure measuring device (**Fig. 6**) used during the measurement [12]:

 Electric Noise Level Meter: UT352 (Uni-Trend Technology Co.);



Figure 5. Used fire alarm sounder, source: own photo

- Sensor element: precision condenser microphone;
- measuring range: 30÷130 dB (A);
- accuracy: 1,5 dB (A);
- Compliance with EN61326:1997+A1:1998 +A2:2001 +A3:2003, EN61672-1:2002 Class 2 and IEC60641:1979 Type 2, ANSI S1.4:1983 Type 2



Figure 6. Used UT352 digital noise level measuring instrument, source: own photo

The measurement was carried out for a total of ten doors. The most relevant information and results are summarized in **Table 2**. The result of the 10th measurement was not used, as the door under test was installed but did not contain a seal, and the result is therefore not considered relevant.

In the **Table 2** the L1 value is the sound pressure level at the open door, 1 m from the sound source. L2 is the sound pressure level value at 1 m on the other side of the door.

Door 6 had the lowest sound reduction, while Door 2 exhibited the greatest soundproofing ability. The glass sliding door of the printing room (No. 6) showed a sound pressure of only 21.1 dB(A), while the No. 2 aluminium-framed glass door showed a lower sound pressure of 43.7 dB(A) on the other side of the door.

Table 2. Result of measurement for testing the fire alarm-related sound insulation properties of interior doors

Door	Room	Width	L1	L2	SPL
<i>No.</i> ,	type	of	[dB]	[dB]	diffe-
type*		doors			rence
		[cm]			[dB]
1.	office	4	103.5	74.8	28.7
2.	office	4,5	104.3	60.6	43.7
3.	meeting	4,5	104.3	62.8	41.5
4.	kitchen	4	104.9	82.6	22.3
5.	corridor	4	105.2	76.8	28.4
6.	printer	4	106.6	85.5	21.1
7.	meeting	4,5	106.3	72.1	34.2
8.	meeting	4,5	105.3	80	25.3
9.	office	4	106	79	27
10.	vestiary	4,5	106.1	82.2	23.9

- * 1. decor foil, hollow inside /old
 - 2. aluminium door frame, glass insert/new
 - 3. aluminium door frame, glass insert/new
 - 4. decor foil, hollow inside / new
 - 5. decor foil, hollow inside /new
 - 6. decor foil, glass sliding door /new
 - 7. metal, glazed /old
 - 8. painted steel sheet door /old
 - 9. HDF wood panel covering, paper grid insert, glass/old
 - 10. decor foil, hollow inside, grey /new

The doors with the smallest and highest sound attenuation are shown in **Fig. 7**.



Figure 7. Tested doors no. 6 and no. 2, source: own photo

Evaluating the results of the measurements (**Fig. 8**), the authors concluded that even in the case of doors with not particularly high soundproofing properties, a higher sound pressure reduction should

be expected compared to the value of $20\,dB(A)$ used in the design (indicated by a red horizontal line in Fig. 8).

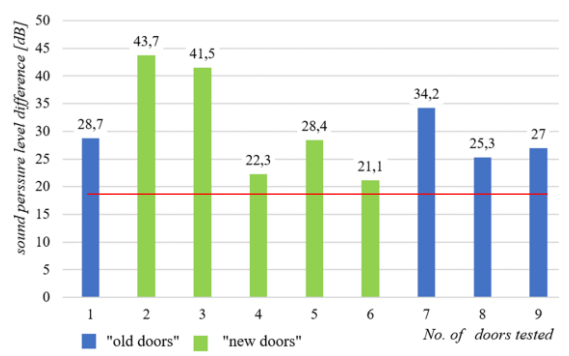


Figure 8. SPL differences between L1 and L2 measure points, source: own figure

The measured level of sound insulation was around 30 dB on average for all the doors tested. In case of the older doors, it was slightly lower, averaging 28.8 dB(A), and for the newer doors it was somewhat higher, averaging 31.4 dB(A).

Interior doors play a role in the complex perception of fire safety, as they delay the spread of fire in their closed state. However, in terms of the audibility of fire alarms, the opposite effect is true. Close doors have the potential to increase the ASET and therefore reduce the occupants' chances for escape. Although fire alarm sounders are designed with the assumption that the doors are closed, in reality some doors are regularly left open. In a domestic environment, for example, the probability of doors being closed has already been investigated. There is a higher probability (on average approx. 60%) of doors being open in a house or apartment. [13] Of course, this is not the same value in the case of different building functions.

III. CONCLUSIONS

This article aim was to examine how the construction industry practice of the past decades, the new technological procedures and materials appearing because of the changed customer expectations influence the efficiency of sound alarm systems distributed according to traditional design practice.

To what extent this trend affects the practice of the sound alarm system's designers. It is necessary to considering an important question among other things, whether the current design attitude needs to be changed or refined. Even though a sound pressure measurement must be carried out before handing over a completed system, proper design practice cannot be based only on verification with subsequent measurements.

By carried out on-site measurements, it was verified that one of the design principles used in

engineering practice, is no more correct. The measurement results confirmed the assumption that the use of doors with better soundproofing in recent years may have a negative effect on the fire alarm in a building. The tests confirmed that the soundproofing properties of the doors should become more important information in the future, which has a strong influence during the design of fire alarm systems. In addition to the usual data services, the authors recommend the designers requesting this information (acoustic rating of the interior doors) in advance from the architect or checking it in the consignment plan.

In addition, an interesting question is whether during operation the audibility of the fire alarm is considered in connection with the replacement of a door with a newer door with higher soundproofing properties. Given that the replacement of interior doors is not a permit-required conversion, awareness is expected from the facility manager and the maintainer of the fire alarm system.

REFERENCES

- [1] L. Moore and J. Kast, "Wily welfare capitalist: Werner von Siemens and the pension plan," *Cliometrica*, Vol. 4, pp. 321-348, 2009.
 - https://doi.org/10.1007/s11698-009-0048-x
- [2] J. A. Tarr, "The municipal telegraph network: origins of the fire and police alarm systems in American cities," *FLUX Cahiers scientifiques internationaux Réseaux et Territoires*, Vol 9, pp. 5-18, July-September 1992.
 - https://doi.org/10.3406/flux.1992.930
- [3] P. J. DiNenno, H. E. Nelson and F. W. Mowrer, SFPE Handbook of Fire Protection Engineering, Third Edition, Quincy Massachusetts Bethesda Maryland: National Fire Protection Association, Society of Fire Protection Engineers, 2002.
- [4] Fire Protection Technical Guideline 5.4.:
 Planning, design and installation of fire
 alarm systems, Hungary Budapest: National
 Directorate General for Disaster
 Management, Ministry of the Interior
 (NDGDM), 2024. Available:
 https://katasztrofavedelem.hu/10502/beepitett-tuzjelzo-berendezes-tervezese-telepitese
 (last acceesed: 02/02/2024)
- [5] EN 54-3 Fire detection and fire alarm systems Part 3: Fire alarm devices Sounders, Brussels: CEN, 2001.
- [6] A. Bowyer, H. Butler és J. Kew, "Locating fire alarm sounders for audibility BSRIA," 81Building Services Research and

AUTHOR CONTRIBUTIONS

Á. Zs. Mohai: Conceptualization, Experiments, Writing and Editing

B. Elek: Theoretical analysis, Review and editing

DISCLOSURE STATEMENT

The authors declare that they have no known competing financial interests or personal relationships that could have appeared to influence the work reported in this paper.

ORCID

Ágota Zsuzsanna Mohai https://orcid.org/0000-0002-6762-5625

Barbara Elek https://orcid.org/0000-0001-7515-6374

- *Information Association, Guildford*, 1981. Available:
- https://www.thenbs.com/PublicationIndex/ Documents/Details?Pub=BSRIA&DocId=2 84767 (last accessed: 19/10/2023)
- [7] "Attenuation of Smoke Detector Alarm Signals in Residential Buildings," Division of Building Research, National Research Council Canada, Ottawa, 1986. Available: https://nrc-publications.canada.ca/eng/view/ft/?id=a2765522-73ad-4aab-b62b-b757083b60b0 (last accessed: 10/10/2023)
- [8] P. Havey, M. Munoz, M. S. Klassen, M. M. Holton és S. M. Olenick, "Variability and Error Rates in Fire Alarm Audibility Measurements and Calculations," *Fire Technology*, Vol 54, pp. 1725-1744, 2018. https://doi.org/10.1007/s10694-018-0755-6
- [9] "Soundproof Door Market Size Growing and Forecasted for period from 2024 2031 and provides complete market analysis of this market," Impulse Insight, 2024. Available:

 https://www.linkedin.com/pulse/soundproof-door-market-size-growing-forecasted-period-lcvke/ (last accessed: 08/12/2023)
- [10] EN ISO 10140 Acoustics. Laboratory measurement of sound insulation of building elements., Switzerland: International Organization for Standardization, 2016.
- [11] "Hosiden Besson," Hosiden Besson Ltd, [Online]. Available: https://hbl.co.uk/app/uploads/2016/01/bans

- <u>hee_excel_lite.pdf</u>. (last accessed: 19/10/2023).
- [12] "UNI-T," Uni-Trend Group Limited, 2008. [Online]. Available: https://meters.uni-trend.com/product/ut352/#Docs. (last accessed: 20/01/2024).
- [13] C. Hopkin, M. Spearpoint és Y. Wang, "Internal door closing habits in domestic premises: Results of a survey and the potential implications on fire safety," *Safety Science*, Vol 120, pp. 44-56, 2019. https://doi.org/10.1016/j.ssci.2019.06.032
- [14] DIN VDE 0833-3 Alarm systems for fire, intrusion and hold-up Part 3: Requirements for intrusion and hold-up

- *alarm systems*, Berlin: Beuth Publishing House, 2020.
- [15] NFPA 72, National Fire Alarm and Signalling Code, USA: NFPA, 2022.
- [16] BS 5839-1 Fire detection and fire alarm systems for buildings Part 1: Code of practice for szstem design, installation, comissioning and maintenance, UK: British Standards Institution, 2017.
- [17] Fire Protection Technical Guideline 2.6.
 Evacuation, Budapest Hungary: National
 Directorate General for Disaster
 Management, Ministry of the Interior
 (NDGDM), 2024. Available:
 https://katasztrofavedelem.hu/315/kiurites
 (last accessed: 03/02/2024)

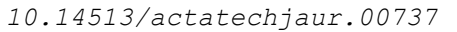


This article is an open access article distributed under the terms and conditions of the Creative Commons Attribution NonCommercial (CC BY-NC 4.0) license.

AJ

ACTA TECHNICA JAURINENSIS

Vol. 17, No. 2, pp. 91-103, 2024





Research Article

Belt tension measurement and monitoring of load securing straps by using resistive stitch-based strain sensors

Norman Lesser^{1,*}, Bernd Sadlowsky²

¹ Institute for BFSV, Ulmenliet 20, 21033 Hamburg, Germany

² HAW Hamburg University of Applied Sciences, Department of process engineering, Ulmenliet 20, 21033

Hamburg, Germany

*e-mail: lesser@bfsv.de

Abstract: This paper focusses on the evaluation of stitch-based strain sensors suitability for the belt tension measuring and monitoring of load securing straps in road freight transportation. Formerly developed stitch-based strain sensor applications were embroidered on a commercial load securing strep, compliant with established industrial standards for load security in the Federal Republic of Germany. The applications were tested in lashing experiments, simulating the securing of a dummy load in road freight transportation. The experiment results showed that they are capable of measuring and monitoring applied amounts of belt tension with a computable change in stitch-resistance. However, cyclic belt tensioning causes strain wear on the stitched applications, resulting in resistance and sensitivity drift.

Keywords: smart textiles; strain sensor; lashing strap; load security

I. Introduction

The proper utilization of narrow fabric load securing straps is essential for an effective cargo security concept in modern road freight transportation. Not properly secured load has been proven to be a high-risk factor in road traffic, causing fatal road accidents. [1]

In recent years various research and development projects have successfully implemented stitch-based textile resistive strain sensors in various substrates, especially in medicine and healthcare applications. [2 - 3] However, the use of stitch-based strain sensors to monitor the belt tension applied to road freight transportation load securing straps has not been researched in depth so far.

In a past conducted research work, two stitch-based strain sensor applications were successfully developed to measure and monitor the strain induced elongation of different woven narrow fabric lashing straps. The stitch-based sensors enabled the strain measurement with the achieved level of strain sensitivity, depending mostly on the individual fabric's deformation characteristics. However, the stitched narrow fabrics weak recovery characteristics have been found to be a crucial

limiting factor for the developed stitch-based strain sensors recovery abilities. [4]

Woven load securing lashing straps must provide good fabric recovery properties to be certified as safe for road transportation in the Federal Republic of Germany. With this main limiting factor expectedly less significant, strain measurement and monitoring may be an interesting use case for the former developed stitch-based strain sensors to possibly enhance road freight load security in future applications.

II. BACKGROUND

Load securing straps are woven narrow fabrics with attached fastening elements like metal hooks, ratchets, or rings. The straps are fastened and tensioned by an operator during the load securing procedure. During transportation a vehicle accelerating, braking, maneuvering or vibrating conducts dynamic acceleration force to the transported load. If the conducted acceleration force is great enough to exceed the loads grip on the ground, it may topple, fall over, hop, or move uncontrolled otherwise, causing damages to the load or even road traffic accidents. The load tensioned securing straps compensate the transport vehicles acceleration by exerting tensile force to the load. During load securing the necessary amount of belt

tension [daN] must be calculated concerning a loads individual mass, size, and shape. In the Federal Republic of Germany, the established industrial standards *VDI 2700* and *DIN EN 12195-1:2021* describe proper calculation and documentation methods and means of securing procedures. [5 - 7] Those standards serve as benchmarks in legal jurisdiction to assess the correctness of load securing in the possible event of a legal claim, should transport damages to the load or a road traffic accident occur. [8]

Woven load securing straps for road freight transportation must meet the proscribed manufacturing and safety requirements of the standard DIN EN 12195-2:2000 to be compliant with VDI 2700 and DIN EN 12195-1:2021. A standard compliant load securing strap must be labelled with its maximum Lashing Capacity (LC). The maximum Lashing Capacity (LC) is a safety limit for the maximum belt tension to be applied to a securing strap during normal use. The safety requirements for woven load securing straps proscribe that a strap tensioned to its labelled Lashing Capacity (LC) shall not elongate more than up to $\varepsilon=7\%$ in the direction of pull and shall show no permanent elongation or damages afterwards. This leads to compliant load securing straps being expected to show good fabric recovery abilities and resistance against permanent deformation at a level of applied belt tension below the labelled Lashing Capacity (LC). [9] VDI 2700 strongly recommends to methodically measure and monitor securing straps belt tension during the ongoing transport to ensure the maintenance of the straps proper tensioning over long transport periods. [10] For measuring and monitoring securing straps belt tension, various analogue and digital measurement tools are commercially available. However, a full textile stitch-based strain sensor application integrated direct into a securing strap does not by now.

Stitching techniques like sewing and embroidery are some of the oldest procedures to join and functionalize textile fabrics. A stitch is built by penetrating needle guiding a sewing thread thru a textile fabric. Modern CNC embroidery machines offer smart textile product developers a broad freedom in the design of aesthetic and functional Textile products stitched patterns. can functionalized during various stages stitchmanufacturing, enabling the based functionalization of pre-finished textile products like load securing straps. A stitch is commonly classified by established standards like ISO 4915:1991, concerning its loop formation and its geometrical properties like stitch length, width, and depth. [11 -131

A stitch made from one or multiple conductive yarns has a specific electrical resistance $[\Omega]$ in relaxed condition. Conductive yarns are mostly spun

from myriads of single conductive staple fibres or filaments. A conductive piece of yarn can therefore be depicted not as an isotropic ideal conductor, but more as a conductive network of an infinitesimal high number of series and parallel circuiting single conductors, physically entangled with one another. In general, a piece of conductive yarns absolute electrical resistance $[\Omega]$ increases with its physical length. For a stitch, this means that its absolute resistance per meter is likely to increase dependent on the total length amount of stitched conductive yarn. The adjustment of stitch properties influencing the final length amount of stitched yarn therefore greatly influences a stitch's absolute electrical resistance. [14-18]

Depending on a stitches property like its width and density, sections of conductive yarn may touch or overlap at the substrates surface. Those physical contact points cause the stitched conductive yarn sections to short-circuit when not proper isolated. While a stitch's overall absolute resistance is likely to increases with an increasing total length amount of stitched conductive yarn, a high concentration of short-circuiting contact points has been found to reduce it. A Stitch is therefore best depicted as a complex conductive network whose overall electrical resistance $[\Omega]$ in relaxed state is an equilibrium of the factors of yarn length to the concentration of short-circuiting yarn contact areas.

When mechanical strain is applied to a stitched fabric, its deformation causes the stitches conductive network to shift. The resistance of a stitches conductive network changes due to its rearrangement, caused by the substrate fabrics elongation. Overlapping and cross sectioning yarn areas may separate from another and cross sectioning areas may shift in contact size and localisation. The short-circuiting contact areas eventually open, turning the conductive networks equilibrium to alter and the stitch's absolute resistance to increase or to decrease. (Fig. 1)

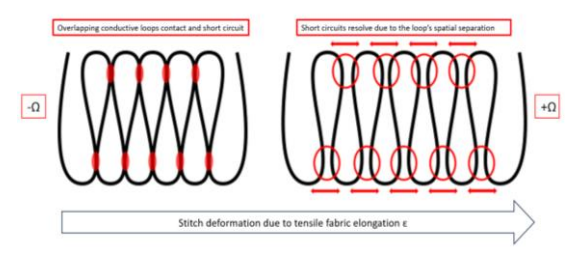


Figure 1. Schematic representation of shortcircuits resolving due to physical yarn separation

The fabrics and stitches deformation may induce mechanical stress to the stitched conductive yarn as well, causing single spun conductive fibres to break or their conductive surface coatings to crack. A damaged conductive yarn may experience a drift in its resistive characteristics, therefore causing the whole stitch's conductive network to alter. [19 - 25]

A measurable resistance change of a stitch-based strain sensor can be used to calculate the stitched fabrics elongation. The calculation method uses the sensors strain sensing gauge factor. The gauge factor K is a proportional factor depicting the sensors grade of resistance change in comparison to its elongation. (Eq. (1) - (3))

$$K = \frac{\frac{\Delta R}{R0}}{\frac{\Delta l}{I}} \tag{1}$$

$$\frac{\Delta R}{R0} = \frac{k \cdot \Delta l}{l} = k \cdot \varepsilon \tag{2}$$

$$\varepsilon = \frac{\Delta l}{l} = \frac{\frac{\Delta R}{R0}}{k} \tag{3}$$

where K = gauge factor; R0 = Resistivity [Ω]; l = length [mm]; ϵ = elongation [%].

The gauge factor is widely established in the use of commercial strain gauges and has been used in various past research to indicate a stitch-based strain sensors general level of strain sensitivity. Other important factors are a strain sensors linearity and especially its recoverability. [22, 26 - 28] A past conducted experiment suggested that a stitched yarns orientation angle in the applied strain force direction directly influences the strain sensors overall resistance and sensitivity drifting characteristics, due to the total amount of conducted mechanical stress likely being dependent on the yarn orientation. Therefore, it's important to consider that a stitchbased strain sensors sensing characteristics are the result of three main aspects interacting with one another. Those being the stitches conductive network shifting under deformation as well as the yarns drifting behaviour and the stitched substrates fabric deformation properties. [4]

III. PROBE PREPARATION

A commercial *DIN EN 12195-2* compliant cargo load securing strap was chosen as a substrate for testing the stitch-based strain sensor applications. (**Fig. 2**) The chosen securing strap is named *Ratschenzurrgurt 1000daN Orange* in this report, after its original product name given by the supplier (*Lasi24 GmbH, Rostock (GER)*). The strap consisted of two narrow fabrics, connected with a supplied metal ratchet for belt tensioning and fixation. The belts technical specifications are given in **Table 1**. The stitch properties are given in **Table 2** and illustrated in **Fig. 3** – **Fig. 7**. All probes were embroidered with loose ends for contacting with a multimeter for resistance measurement.

Table 1. Technical specification Ratschenzurrgurt 1000daN Orange

Belt pieces	2 pieces (1* loose end and 1* fixed end)
Total belt length	4000mm
Fixed end length	500mm
Loose end length	3500mm
Belt thickness	35mm
Belt width	2mm
Fixation belt- attachment	Metal hooks
Belt fastener	Metal ratchet
Maximum Lashing capacity LC	1000daN
Elongation at Maximum Lashing capacity LC	<7%
Fibre Material	100% PES

The Load securing straps were embroidered with two versions of an *ISO 4915:1991* 304-ZigZag lockstitch using a *ZSK JCZA* computer-controlled embroidery machine (*ZSK Stickmaschinen GmbH, Krefeld (GER)*). Both applications dimensions are illustrated in **Fig. 3**. Both stitches were developed in a research work prior [4]

Table 2. Stitch properties

Stitch Version	Stitch density	Stitch width	Stitch depth
ZigZag_V2_Axial	11 Stitches /10mm	5 mm	0.9 mm
ZigZag_Double_V2	8 Stitches /10mm	0.8 mm	1.2 mm

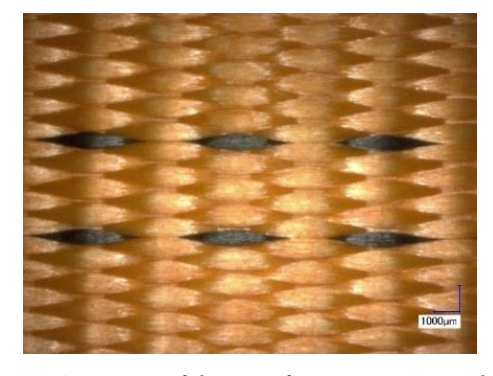


Figure 2. Narrow fabric surface image "Ratschenzurrgurt 1000daN Orange"

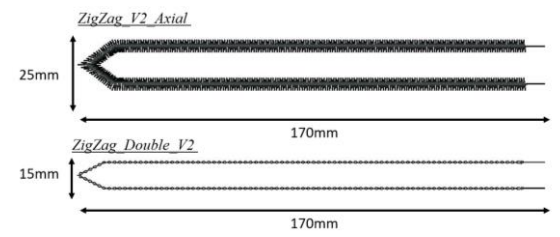


Figure 3. Stitch-dimensions

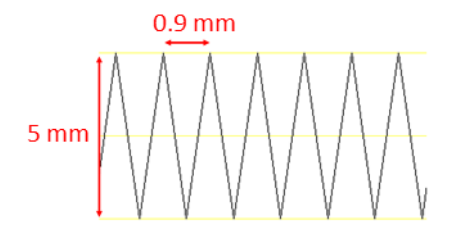


Figure 4. Stitch properties ZigZag_V2_Axial



Figure 5. Microscope image ZigZag_V2_Axial

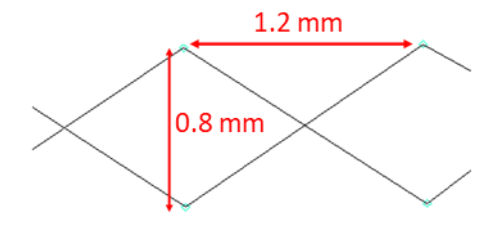


Figure 6. Stitch properties ZigZag_Double_V2



Figure 7. Microscope Image ZigZag_Double_V2

The chosen silver-plated yarn Amann Silver-tech+150 (Amann&Söhne GmbH & Co.KG, Bönningheim (GER)) was successfully used to manufacture stitch-based strain sensors for measuring and monitoring lashing straps belt tension in a previous study. [4] The stitch version of ZigZag_V2_Axial was embroidered using only a conductive upper thread and the non-conductive yarn Amann ISA Tex 80 as a lower thread. In the version of ZigZag_Double_V2 the upper thread and

the lower thread consisted of the conductive yarn *Amann Silver-tech+150.* (**Table 3**)

Table 3. Yarn properties

Yarn	Fiber material	Titer [dtex]	Yarn resistivity [Ω/m]
SIlver- Tech+150	100% PA	220	<300
ISA Tex 80	100% PES	180	-

IV. TESTING METHOD

To judge the developed strain sensors usability for load securing applications it was decided to design experiments as close to a reality as possible. For testing the stitched applications capability to measure and monitor the applied belt tension, a cyclic tensioning experiment and a long-term lashing testing experiment were conducted. Both experiments were inspired by common use cases of load securing straps in road freight transportation.

Two dummy loads, consisting of 7 wooden EN 13698 compliant load carrier palettes (LxWxH = 1200mm x 800mm x 140mm) were stapled onto one another. The total size of the two dummy loads was $LxWxH = 1200mm \times 800mm \times 850mm$. The dummy loads were exposed to climatization 20°C/65% rel. humidity for 24 hours in an accessible climate chamber together with the stitched load securing straps. After climatizing, the stitched load securing straps were used to lash 6 of the palettes onto the lowest seventh palette. (Fig. 8) The probes stitch applications were positioned free-floating approximately in the middle above the dummy loads' length. The straps were orientated in the same direction while lashing so the stitch applications pointed in the same direction. Edge protectors made of cardboard were put between the lashing straps and the upper palettes edge to protect the straps from abrasion. (Fig. 9)



Figure 8. Lashed dummy load



Figure 9. Positioned strain sensor applications



Figure 10. Measurement of the probes electrical resistance (left) and belt tension (right)

For fastening the strap's attached metal hooks were hooked into the lowest wooden palette. The securing straps were tensioned using the attached metal ratchets. For measuring the belt-tension the belt tension measuring tool TENMET 500 (GWS®-Schlobohm, Zeven (GER)) was used. The conductive stitches electrical resistance $[\Omega]$ was measured with a DMM6500 6 ½ Multimeter (Keithley Instruments Inc., Cleveland (USA)). (Fig. 10)

The cyclic tensioning experiment was designed to simulate the multiple use of a functionalized load securing straps lashing down the dummy loads multiple times. The stitched lashing straps were successively tensioned from 0daN to 100daN and to 200daN without loosening in between. The cycle was repeated 5 times in total. The stitch applications electrical resistance $[\Omega]$ was measured before tensioning as well as 30 seconds after reaching 100daN and 200daN. At each cycles end the straps were loosened by opening the tensioning metal ratchets. Between every tensioning cycle the 10 minutes were waited to give the woven lashing strap enough time for relaxation. Before and after every conducted tensioning cycle the stitch applications length was measured using a steel measurement ruler. This was conducted to detect a possible permanent stitch elongation. In each cycle the probes strain sensitivity measured by calculating the strain gauge factor.

The described testing method didn't allow a precise measurement of the narrow fabric elongation $[\varepsilon]$ during the belt tensioning procedure. For reference unstitched probes of the used load securing strap were tested for their tensile strength according to DIN EN ISO 13934-1 with a Zwick Allroundline

Z100 tensile testing machine, a 50kN Xforce K loading cell and a VideoXtens elongation transducer (ZwickRoell GmbH & Co. KG, Ulm (GER)). The tensile testing procedure was conducted using a 50kN roller specimen holder Type 8564 (ZwickRoell GmbH & Co. KG, Ulm (GER)). For measurement data gathering the program TextXpert 3 was used. The tensile testing procedure was conducted by ZwickRoell GmbH & Co.KG.

For reference testing 3 unstitched probes of the strap $Ratschenzurrgurt\,1000daN\,Orange$ were tested until rupture. From the gathered data the straps average elongation [ϵ %] was calculated at 100daN and 200daN applied tension force. The averaged elongation percentages were used for reference to calculate the probes strain gauge factors as an indicator for the strain sensitivity.

The long-term lashing experiment was designed to simulate a load being lashed down for a long transport duration. The dummy loads were lashed down with 200daN applied belt tension. The lashed loads were left unmoved in the climate chamber under constant 20°C/65% rel. humidity climate exposure for 48 hours in total. The stitches electrical resistivity was measured after 12 hours, 24 hours, 36 hours and after 48 hours alongside the belt tension. With this procedure the stitched applications ability to monitor the straps applied belt tension and possible belt tension loosening overtime were tested. All stitched applications lengths were measured before both experiments and 24 hours after completion in a 20°C/65% rel. humidity-controlled climate environment. For the length measurement a steel ruler was used. (Fig. 11)



Figure 11. manual application length measurement

It is important to note, that both experiments were conducted inside of a climate chamber and in a stable climate environment 20°C/65% rel. humidity to minimalize climate fluctuations for the duration of this research work.

V. RESULTS

In this section the cyclic tensioning and the long-term lashing experiment's results are presented. The cyclic tensioning experiment's results show that both stitch applications enable the measurement of the applied levels of belt tension by a distinctive change in electrical resistance $[\Omega]$.

The reference tensile tests of the unstitched securing straps resulted in an averaged elongation of ε =0,57% at 100daN and ε =0,84% at 200daN applied tensile force. This elongation values were used to calculate the probes gauge factors during cyclic tensioning. In the first cycle the probes based on $ZigZag_Double_V2$ show an averaged gauge factor of 5,3 at 100daN and 8,71 at 200daN belt tension. The probes based on $ZigZag_V2_Axial$ had an averaged gauge factor of 5,32 at 100daN and 7,25 at 200daN belt tension. (**Fig. 12** – **Fig. 13**)

The probes of both stitches experience a cyclic electrical resistance drift and a cyclic sensitivity drift. The measured electrical resistance at 0daN, 100daN, and 200daN belt tension increases after each conducted tensioning cycle. (**Fig. 14** – **Fig.15**) The relative resistance drift related to the first cycle is shown in **Fig. 16** and **Fig. 17**. The ZigZag_Double_V2 probes relative resistance drift is slightly higher than ZigZag_V2_Axial and both the absolute and relative drift curves indicate a comparatively more volatile resistance drifting behaviour. However, both applications show a largely similar positive electrical resistance curve progression.

The sensitivity drifting behaviour deviates more significantly between both stitch applications than the observed electrical resistance drift. The $ZigZag_V2_Axial$ based Probes display a strong gauge factor drop after the first conducted cycle. Between the following cycles the level of sensitivity remains then on a reasonable stable plateau. However, ZigZag_Double_V2 shows a much more volatile sensitivity drifting behaviour.

During the long-term lashing experiment all stitched securing belts display a continued belt tension loosening. The straps belt tension loosening is accompanied by a decline of both stich applications electrical resistance. While the probes belt tension curve progresses in a similar regressive pattern, the electrical resistance curve progression pattern diverges. (Fig. 18 - Fig. 19)

The probes based on ZigZag_V2_Axial exhibit a regressive electrical resistance curve progression during the experiment. The curves correspond well with the belt tension loosening curve progression. ZigZag_Double_V2 however shows an electrical resistance curve progression less regressive and less corresponding to the belt tension loosening.

The conducted length measurements before and after both experiments indicate no clearly measurable permanent stitch deformation. However, all probes show a permanently increased electrical resistance in relaxed state. (**Table 4** – **Table 7**)

Table 4. ZigZag_Double_V2 – Cyclic tensioning experiment

Probe	A	В	С	D	E
Δ1	0	0	0	0	0
Ωl_0	45.56	43.8	44.9	46.9	50.23
$\Omega 1_1$	46.91	45.91	50.8	54.12	56.07
$\Delta\Omega$	1.35	2.11	5.9	7.22	5.84
$\Delta\Omega$ [%]	+2.95%	+4.82%	+13.14%	+15.39%	+11.63%

Table 5. Cyclic ZigZag_V2_Axial - Cyclic tensioning experiment

Probe	A	В	C	D	\boldsymbol{E}
Δ1	0	0	0	0	0
$\Omega 0$	2088	2157	2113	2024	2029
Ω1	2159	2264	2248	2107	2111
$\Delta\Omega$	71	107	135	83	82
$\Delta\Omega$ (rel.)	+3.40%	+4.96%	+6.39%	+4.10%	+4.04%

Table 6. ZigZag_Double_V2 – long-term lashing experiment

Probe	A	В	C	D	E
Δ1	0	0	0	0	0
$\Omega 0$	47.39	49.03	51.65	43.71	48,12
Ω1	48.11	49.86	52.04	44.23	48.57
ΔΩ	0.72	0.83	0.39	0.52	0.45
$\Delta\Omega$ (rel.)	+1.52%	+1.69%	+0.76%	+1.19%	+0.94%

Table 7. ZigZag_V2_Axial - long-term lashing experiment

Probe	A	В	C	D	E
Δ1	0	0	0	0	0
$\Omega 0$	2063	2119	2071	2099	2104
Ω1	2079	2141	2108	2107	2121
$\Delta\Omega$	16	22	37	8	17
$\Delta\Omega$ (rel.)	+0.78%	+1.04%	+1.79%	+0.38%	+0.81%

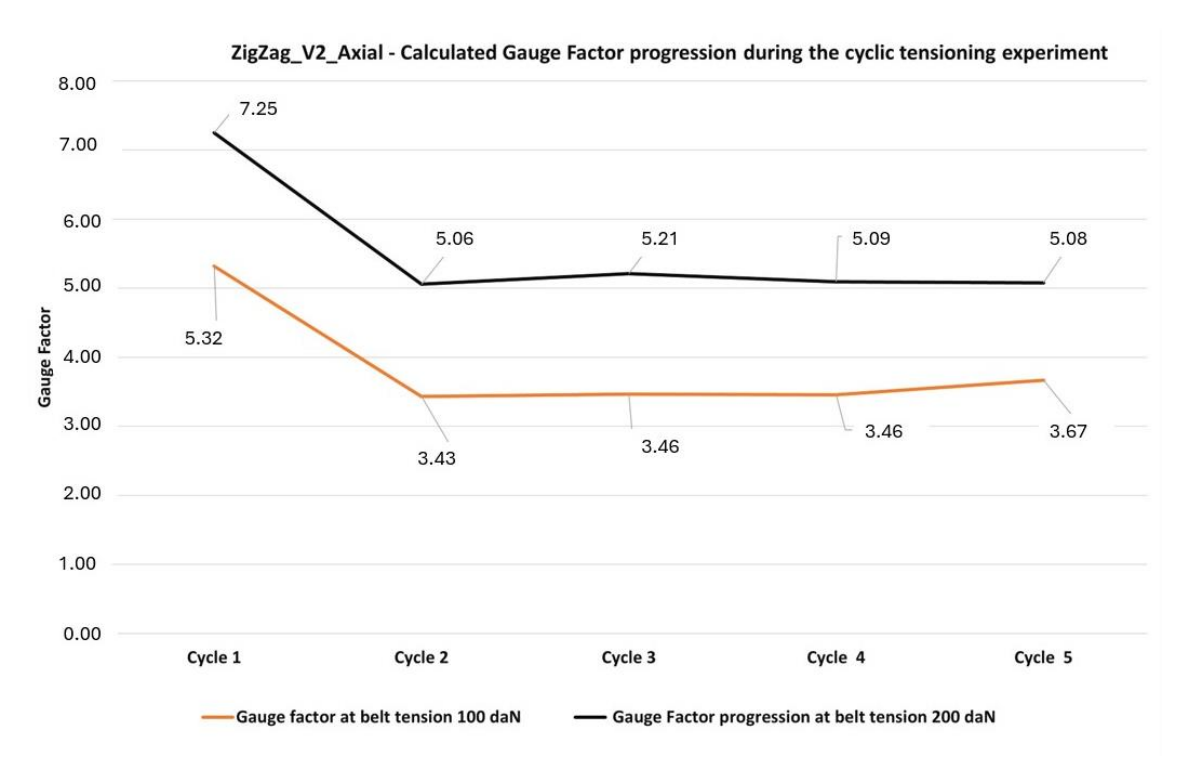


Figure 12. Calculated Gauge Factor progression during the cyclic tensioning experiment – ZigZag_V2_Axial

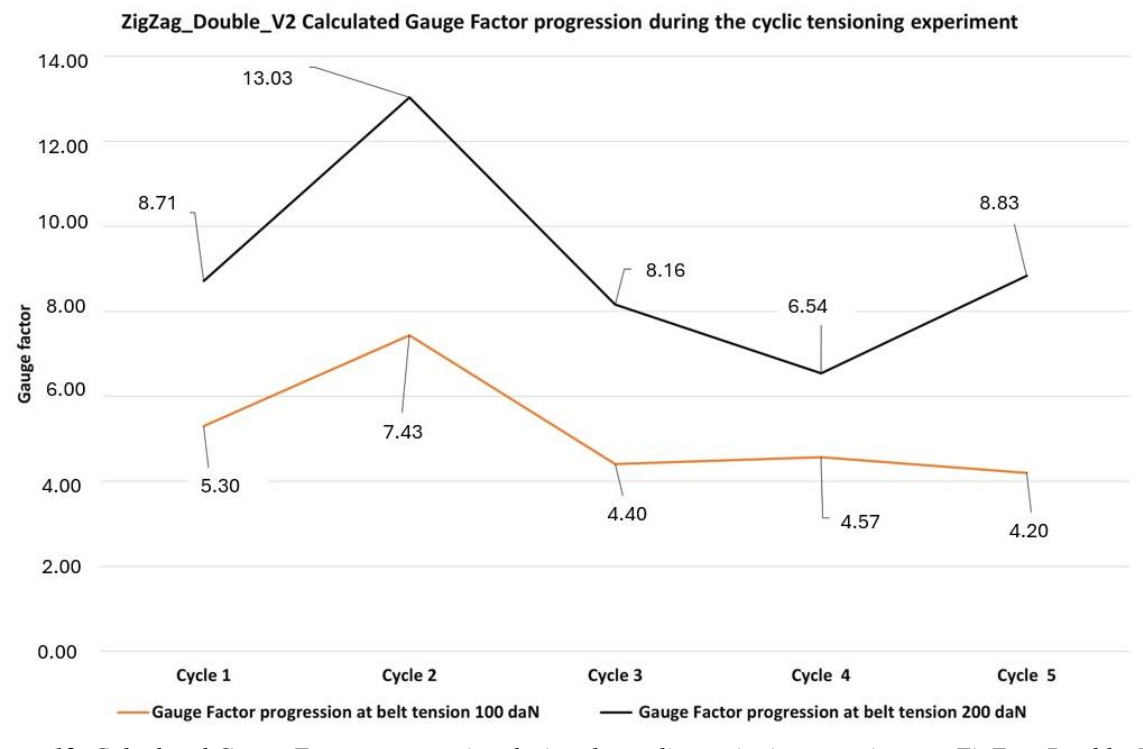
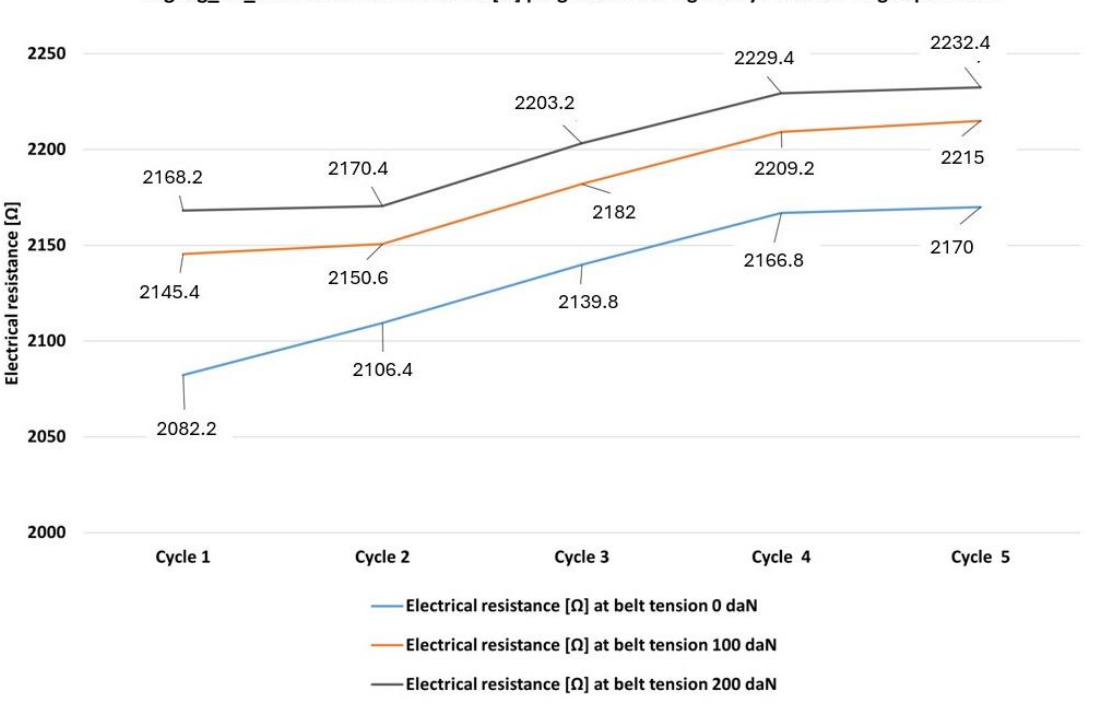


Figure 13. Calculated Gauge Factor progression during the cyclic tensioning experiment – ZigZag_Double_V2



 ${\sf ZigZag_V2_Axial} \ Electrical \ resistance \ [\Omega] \ progression \ during \ the \ cyclic \ tensioning \ experiment$

Figure 14. Electrical resistance $[\Omega]$ progression during the cyclic tensioning experiment – ZigZag_V2_Axial

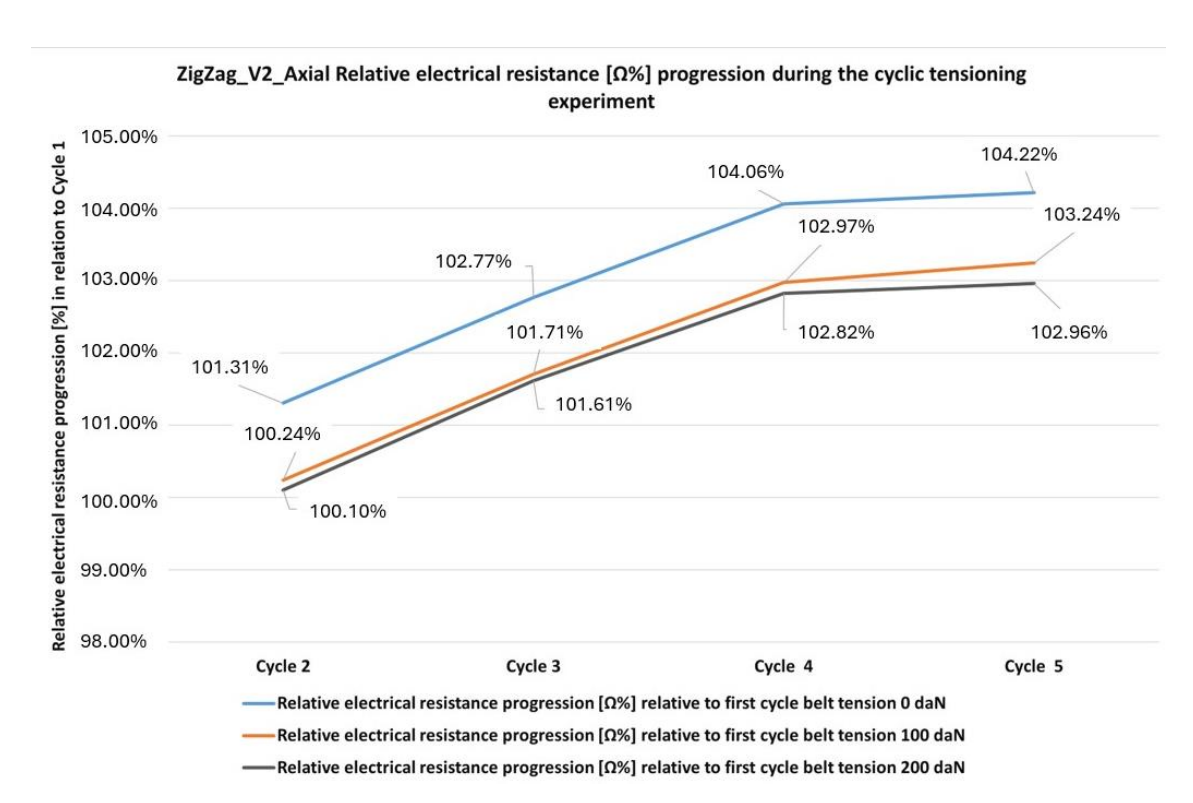


Figure 15 Relative Electrical resistance [Ω %] progression during the cyclic tensioning experiment – $ZigZag_V2_Axial$

ZigZag_Double_V2 Electrical resistance [Ω] progression during the cyclic tensioning experiment

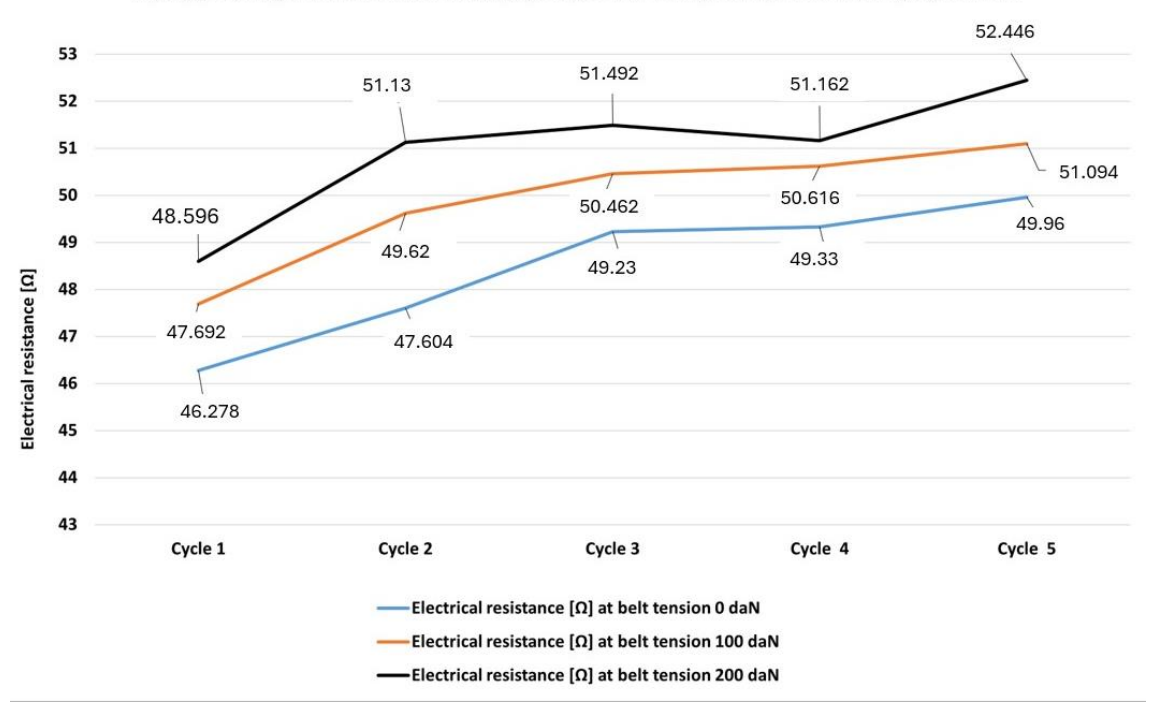


Figure 16. Electrical resistance [Ω] progression during the cyclic tensioning experiment – ZigZag_Double_V2

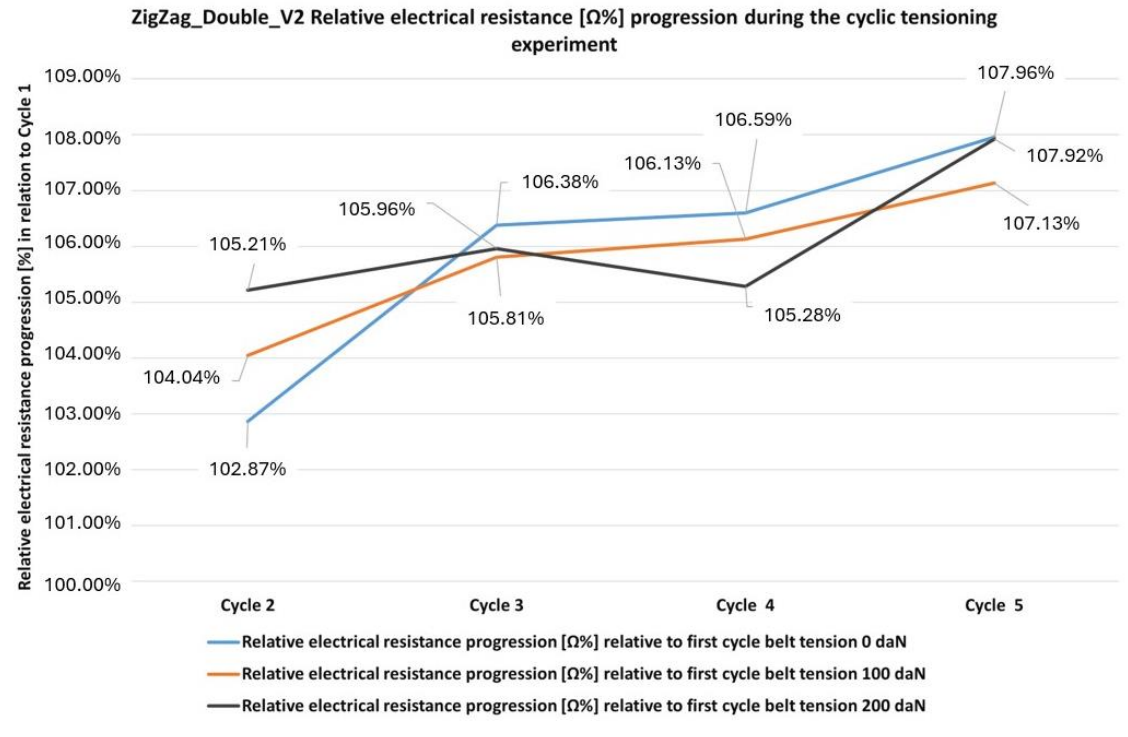


Figure 17. Relative Electrical resistance [Ω %] progression during the cyclic tensioning experiment – $ZigZag_V2_Axial$

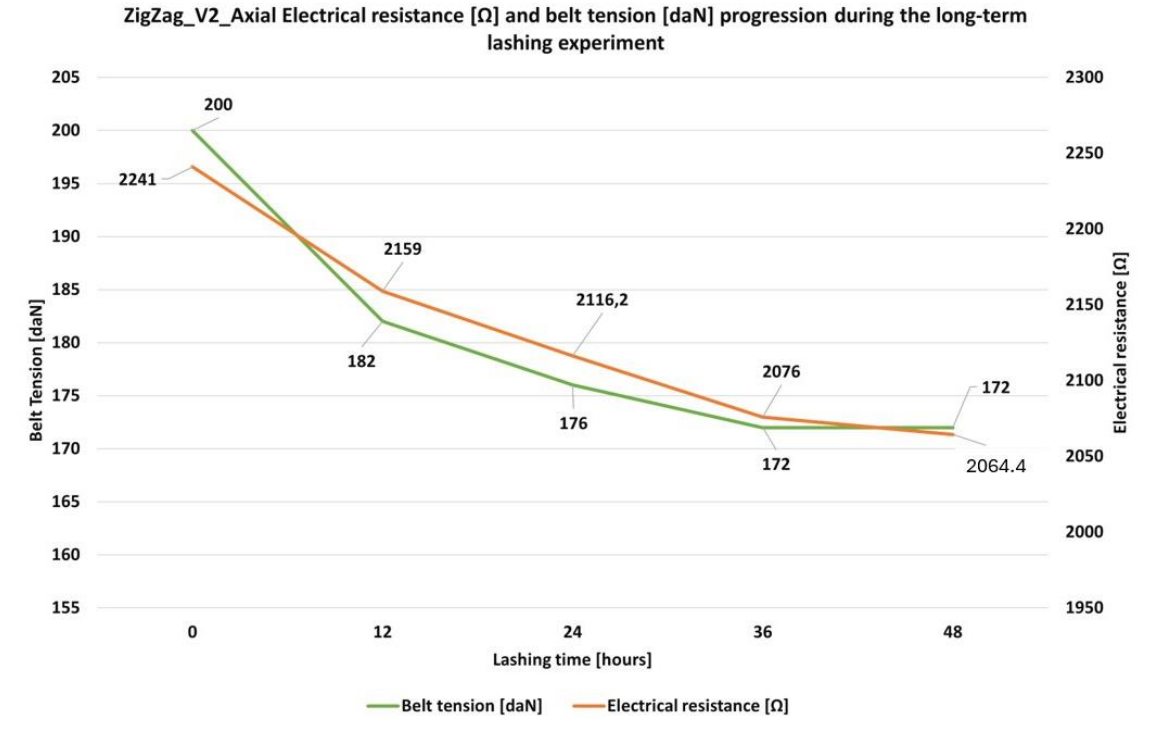


Figure 18. Electrical resistance $[\Omega]$ and belt tension [daN] progression during the long-term lashing experiment $-ZigZag_V2_Axial$

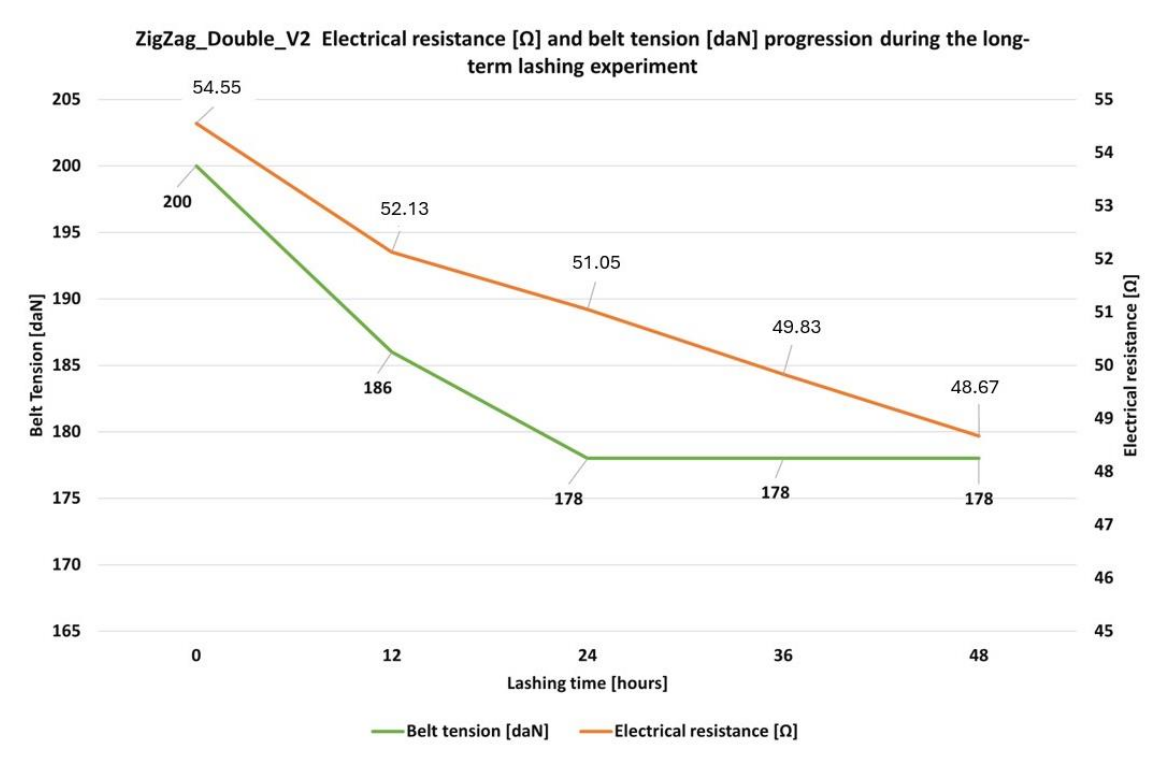


Figure 19. Electrical resistance $[\Omega]$ and belt tension [daN] progression during the long-term lashing experiment - ZigZag_Double_V2

VI. DISCUSSION

The conducted experiments results show that the developed Stitch applications ZigZag_V2_Axial and ZigZag_Double_V2 both enable the measurement and monitoring of belt tension, applied to a standard compliant load securing strap. Both probes displayed clearly distinguishable changes in the electrical resistance corresponding to different levels of belt tension. The cyclic tensioning experiment showed that ZigZag_Double_V2 provides a higher gauge factor compared to ZigZag_V2_Axial in every cycle and at every level of applied belt tension. However, in Comparison ZigZag_Double_V2 displayed a higher and more volatile sensitivity and relative resistance drift. However, ZigZag Double V2 provides higher gauge factors, ZigZag V2 Axial displays a less volatile cyclic sensitivity drift and therefore indicates better recovery properties in comparison.

In the past conducted development work of the two stitch applications, a similar drifting behavior was found. The observed drifting behavior back then was suggested to be especially caused by the combination of the conductive yarns cyclic tensile wear, its orientation angle on the fabric surface and the tested narrow fabrics proneness for permanent elongation. [4]

The load securing strap used in this conducted work however shows good recovery properties with no permanent elongation measurable. With this factor considered expelled the observed resistance and sensitivity drift is very likely to be driven mainly by cyclic tensile wear to the conductive yarn. ZigZag_V2_Axial has a higher stitch length and width than ZigZag_Double_V2. This results in the single stitch sections laying in a lower angle and in a less direct orientation towards the tensile force direction during belt tensioning.

Due to the higher orientation, the conductive yarn is likely more exposed to mechanical stress, resulting in the spun silver-plated polyamide fibers experiencing more intense tensile wear. (Fig. 20) A fibers conductive surface coating cracking or loosing integrity otherwise due to mechanical wear is a commonly expected cause for conductive fibers electrical resistance permanently increasing and the strain sensitivity to alter is described by the so called Crack Modell. [19, 21] The myriads of single spun cracking more severely due ZigZag_Double_V2's yarn higher tensile wear explains the increased and more volatile resistance and sensitivity drift compared to ZigZag V2 Axial.

This suggests that both developed stitchapplications recoverability is limited by the used conductive yarns vulnerability to tensile wear, even in combination with a highly recoverable narrow fabric. Therefore, further modification of the stitch properties influencing the yarns orientation on the fabrics surface and the choose of yarn itself are expected to be key parameters for optimizing a stitch-based strain sensors recoverability in this special use case.

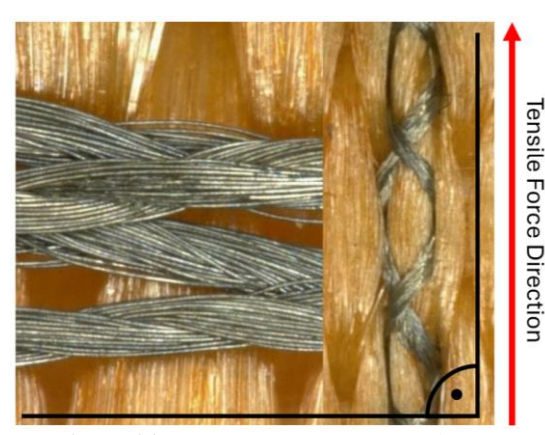


Figure 20. Yarn orientation in tensile force direction (left: ZigZag_V2_Axial; right: ZigZag_Double_V2)

From the long-term lashing experiment results can be conducted, that $ZigZag_V2_Axial$ enables a more precise monitoring of the securing straps losing belt tension. The loss of belt tension can be explained by the fabric progressively rearranging under static deformation to relief tension. The VDI 2700 mentions this behaviour as expectable for load securing straps and therefore strongly suggests ongoing belt tension monitoring over the transport time as a countermeasure. [10]

The measured resistance drop of both stitch applications is likely caused by the fabric's relaxation rearranging the stitches conductive network towards its former relaxed state as well. ZigZag V2 Axial's resistance curve progression corresponds especially well with the securing straps behaviour in comparison to ZigZag Double V2. Due to the high stitch density and stitch width, ZigZag_V2_Axial has a high concentration of shortcircuiting contacting yarn areas. When the fabric and the stitch rearrange towards their original relaxed state, former opened short-circuits may reconnect by yarn areas physically separated during fabric tensioning reconnect to one another. ZigZag_V2_Axials belt tension monitoring ability therefore likely benefits from the application's high concentration of short-circuiting yarn sections opening and reconnecting, in comparison to ZigZag_Double_V2.

The probes based on $ZigZag_V2_Axial$ show a significantly higher absolute initial electrical resistance and higher absolute deltas in measured resistance [$\Delta\Omega$] both conducted experiments, compared to $ZigZag_Double_V2$. This is likely caused by $ZigZag_V2_Axial$'s stitch properties (especially it's high stitch density and length) result

in a bigger total length amount of conductive yarn being stitched onto the substrate.

VI. CONCLUSION

The results of this work suggest that both stitchbased strain sensors enable the belt tension measurement and long-term monitoring of a DIN EN 12195-2 compliant load securing strap. The conducted experiments were designed close to a practical load securing procedure to investigate the stitch-based strain sensors usability in this specific use case. From this viewpoint, ZigZag_V2_Axial is a promising candidate for future development attempts and iterations. ZigZag_V2_Axial in its current iteration is already capable to reproduce the fabric relaxation behavior of a load securing strap with a high degree of accuracy. The measured high absolute resistance deltas enable a precise distinction between different levels of belt tension. Both tested stitch-based strain sensor applications are vulnerable to cyclic resistance and sensitivity drift in their current iteration. This greatly limits the practical use in road freight transportation.

However, the conducted experiments result strongly suggest that the choose of conductive yarn and the yarns orientation influencing stitch properties are the main parameters for further optimization. Using a yarn less vulnerable for tensile wear and further adjustment of the stitch parameters could possibly greatly enhance the stitch-based strain sensors recovery properties in future iterations.

It's important to note that environmental interferences have been mostly left out for the experiments conducted in this research work. During road freight transport numerous interferences like a vehicle's vibration, temperature changes or magnetic fields etc. can possibly greatly influence the stitch-

VII. REFERENCES

- [1] Statista GmbH, German Federal Statistical Office, Anzahl der Straßenverkehrsunfälle mit Personenschaden verursacht durch unzureichend gesicherte oder unangemessene Beladung in Deutschland im Jahr 2019, (2020) [cited:2024-01-27].
- [2] R. Nolden, K. Zöll, A. Schwarz-Pfeiffer, Smart Glove with an Arduino-Controlled Textile Bending Sensor, Textile Data Conductors and Feedback Using LED-FSDs™ and Embroidery Technology, Proceedings, 68 (1) (2021) 4. http://doi.org/10.3390/proceedings202106800
- [3] M. Hoerr, E-Textiles Integration von Elektronik in Textilien durch Stickerei, TEXTILplus (03/04) (2021) pp. 18 22, in German.

based strain sensors behavior and require special kinds of insulation or shielding.

Those aspects must be considered and included in future experiments and research work. However, for better comparison of the results and especially due to limited technical possibilities concerning conducting the described experiments under controlled vibration, it was decided to exclude those factors from this conducted work.

Test equipment with a more precise measurement of belt tension and electrical resistance $[\Omega]$ must be used to further refine and to validate the observed sensor characteristics.

However, CNC-embroidery is a precise manufacturing technology with a high possible grade of automatization. A further developed and validated stitch-based strain sensor could become an interesting alternative for the cheap functionalization of load securing belts and to enhance road freight transportation security in the future.

ACKNOWLEDGEMENT

The publishing of this paper was supported by the BFSV institute of Packaging Hamburg

AUTHOR CONTRIBUTIONS

Norman Lesser: Conceptualization, Experiments, Theoretical analysis, Writing

Bernd Sadlowsky: Supervision and editing.

DISCLOSURE STATEMENT

The authors declare that they have no known competing financial interests or personal relationships that could have appeared to influence the work reported in this paper.

- [4] N. Lesser, B. Sadlowsky, The development of a stitch-based strain sensor for woven lashing straps, Acta Technica Jaurensis, 17 (1) (2024) pp. 22 35.
 - http://dx.doi.org/10.14513/actatechjaur.00728
- [5] Ladungssicherungseinrichtungen auf Straßenfahrzeugen – Sicherheit - Teil 1: Berechnung von Sicherheitskräften, DIN 12195-1, (2021), in German
- [6] Ladungssicherung auf Straßenfahrzeugen, VDI 2700, (2004), in German
- [7] Ladungssicherung auf Straßenfahrzeugen Berechnung von Sicherungskräften Grundlagen, VDI 2700 Blatt 2 / Part 2, (2014), in German
- [8] Federal Republic of Germany German Road Traffic Regulation (StVO) §22, in German

- [9] Ladungssicherungseinrichtungen auf Straßenfahrzeugen – Sicherheit - Teil 2: Zurrgurte aus Chemiefasern, DIN 12195-2, (2000), in German
- [10] Ladungssicherung auf Straßenfahrzeugen Gebrauchsanleitung für Zurrmittel, VDI 2700 Blatt 3.1 / Part 3.1, (2023), in German
- [11] G. K. Stylios, The mechanics of stitching, in: I. Jones, G. K. Stylios, Woodhead Publishing Series in textiles: Number 110 Joining textiles Principles and applications, Woodhead Publishing Limited, Cambridge, (2013), pp.48 51
- [12] Stitches and seams. Classification and terminology of stitch types, ISO 4915:1991, (1991)
- [13] V. Mecnika, M. Hoerr, I. Krievins, S. Jockenhoevel, T. Gries, Technical Embroidery for Smart Textiles: Review, Material Science. Textile and Clothing Technology, 9 (2014) pp. 56-63.

http://doi.org/10.7250/mstct.2014.009

- [14] J. Eichhoff, A. Hehl, T. Gries, Textile fabrication technologies for embedding electronic functions into fibres, yarns and fabrics, in: T. Kirstein, Woodhead Publishing Series in textiles: Number 139 Multidisciplinary knowhow for smart-textiles developers Woodhead Publishing Limited, Cambridge, (2013), pp.193 223.
- [15] L. Xiuhong, S. Chen, Y. Peng, Z. Zheng, J. Li, F. Zhong, Materials, Preparation Strategies, and Wearable Sensor Applications of conductive Fibers: A Review, Sensors, 22 (8) (2022) 3028. http://doi.org/10.3390/s22083028
- [16] J. Xie, M. Miao, Y. Jia, Mechanism of electrical conductivity in metallic fiber-based yarns, AUTEX Research Journal, 20 (1)

(2019), p. 6. http://doi.org/10.2478/aut-2019-0008

- [17] M. Miao, Electrical conductivity of pure carbon nanotube yarns, Carbon, 49 (12) (2011), pp. 3755 3761.
- [18] S. Chawla, M. Narahji, Effects of twist and porosity on the electrical conductivity of carbon nanofiber yarns, Nanotechnology, 24 (25) (2013) 255708. http://doi.org/10.1088/0957-24/25/255708
- [19] F. Huang, H. Jiyong, X. Yan, Review of Fiberon Yarn-Based Wearable Resistive Strain Sensors: Structural Design, Fabrication Technologies and Applications, Textiles, 2 (1) (2022), pp. 81-111.

http://doi.org/10.3390/textiles2010005

[20] K. Keum, S.S. Cho, J. Jeong-Wan, S.K. Park, K. Yong-Hoon, Mechanically robust textilebased strain and pressure multimodal sensors using metal nanowire/polymer conducting fibers, iScience, 25 (4) (2022) 104032.

http://doi.org/10.1016/j.isci2022.104032

[21] S. Seyedin, P. Zhang, M. Naebe, S. Qin, J. Chen, X. Wang, J. M. Razal, Textile Strain Sensors: A Review of the Fabrication Technologies, performance Evaluation and Applications, Materials Horizons, 6 (2) (2019) pp. 219 – 249.

http://doi.org/10.1039/C8MH01062E

[22] O. Tangsirinaruenart, G. Stylios, A Novel Textile Stitch-Based Strain Sensor for Wearable End Users, Materials, 12 (2019) 1469

http://doi.org/10.3390/ma12091469

[23] M. Ruppert-Stroescu, M. Balasubramanian, Effects of stitch classes on the electrical properties of conducive threads, Textile Research Journal, 88 (21) (2017), pp. 2455 – 2463

http://doi.org/10.1177/0040517517725116

- [24] A. Vogl, P. Parzer, T. Babic, J. Leong, A. Olwal, M. Haller, StretchEBand: Enabling Fabric-based Interactions through Rapid Fabrication of Textile Stretch Sensors, in: CHI '17: Proceedings of the 2017 CHI Conference on Human Factors in Computing Systems, New York, (2017) pp. 2617 2627. http://doi.org/10.1145/3025453.3025938
- [25] M. Martinez-Estrada, I. Gil, R. FernándezGarcía, Raúl, An Alternative Method to Develop Embroidery Textile Strain Sensors, Textiles, 1 (3) (2021), pp. 504 512. http://doi.org/10.3390/textiles1030026
- [26] P. Regtien, E. Dertien, Sensors for Mechatronics – Second Edition, Elsevier B.V., Amsterdam, (2018).
- [27] S. Keil, Dehnungsmessstreifen 2. Auflage, Springer Vieweg, Wiesbaden (2017), p. 485, in German.
- [28] A. Schwarz, L. Van Langenhove, Types and processing of electro conductive and semiconducting materials for smart textiles, In: T. Kirstein, Woodhead Publishing Series in textiles: Number 139 Multidisciplinary knowhow for smart-textiles developers Woodhead Publishing Limited, Cambridge, (2013), pp. 28 57.



This article is an open access article distributed under the terms and conditions of the Creative Commons Attribution NonCommercial (CC BY-NC 4.0) license.